JOURNAL OF GEOPHYSICAL RESEARCH, VOL. 96, NO. C8, PAGES 14,885–14,907, AUGUST 15, 1991

Structure and Dynamics of a Coastal Filament

RICHARD K. DEWEY,[1] JAMES N. MOUM, CLAYTON A. PAULSON, DOUGLAS R. CALDWELL, AND STEPHEN D. PIERCE

College of Oceanography, Oregon State University, Corvallis

Repeated microstructure transects across filaments in the coastal transition zone (CTZ) have revealed fundamental structure and dynamics of the complicated features. The measurements allow detailed momentum and vorticity analyses and provide a possible explanations for structural asymmetry of the fronts. Observations made between July 2 and July 23, 1988, along the central meridional CTZ survey line were used to estimate terms in the meridional momentum equation. The analysis indicates geostrophic flow along the axes of the fronts with the across-front pressure gradient explaining as much as 87% of the variance in the balance. Significant ageostrophic flow in the across-front coordinate was found, with the along-front pressure gradient explaining only 71% of the variance in the momentum balance. The fronts were found to be asymmetric in relative vorticity, with stronger positive vorticity on the cooler side of the front and weaker negative vorticity on the warm side. Mean vertical velocities were estimated from the repeated transects of acoustic Doppler current profiles and the rapid sampling vertical profiler hydrographic and turbulence measurements. Regions of upwelling and downwelling are likely associated with adjustments in the relative vorticity, resulting in maximum vertical velocities of 40 m d^{-1}. Asymmetry in the near-surface temperature and salinity extrema are explained by cross-frontal exchange. This cross-frontal exchange modifies the relative roles of salinity and temperature in determining the density away from the coastal upwelling region, a dynamically important characteristic not revealed by advanced very high resolution radiometer imagery.

1. INTRODUCTION

"Squirtlike" structures extend hundreds of kilometers seaward of the California continental shelf. In late spring (April–June) alongshore southward winds over the Oregon and northern California shelf regions induce coastal upwelling that introduces a significant tilt in the isopycnal slopes over the continental shelf [*Huyer and Kosro*, 1987]. The alongshore southward current that develops is referred to as the California Current. Satellite images (e.g., *Flament et al.*, 1985; *Abbott and Barksdale*, this issue; *Strub et al.*, this issue] reveal that the fronts associated with the California Current are not confined to the shelf and upwelling region. Between the central California regions of Cape Mendocino and Point Reyes the fronts undergo large displacements from the continental shelf and often extend hundreds of kilometers seaward of the upwelling region. Processes within this transition zone, bounded by the continental slope and the deep ocean, determine the exchange of properties between coastal upwelling and mid-ocean environments.

Microstructure measurements were collected along the central "D line" of the coastal transition zone (CTZ) hydrographic survey grid [*Huyer et al.*, this issue], west of Point Arena, California. The grid was made up of six alongshore lines (A–F) extending from the shelf break to 100 km seaward of the shelf region. Microstructure measurements included thermistor chain, rapid sampling vertical profiler (RSVP) and acoustic Doppler current profiler (ADCP) profiles, continuous sea surface temperature and conductivity measurements, and hourly meteorological measurements. The microstructure survey was conducted between July 2 and July 23, 1988.

Results from the microstructure pilot cruises in 1986 [*Moum et al.*, 1988] and 1987 [*Dewey and Moum*, 1990] indicated that strong turbulent activity is limited to the surface mixing layer, driven by surface wind stresses. For wind speeds greater than 6 m s^{-1}, *Dewey and Moum* [1990] find that the integrated dissipation rates over the surface mixing layer are significantly correlated with the wind power ($\rho_0 u_*^3$). They also find a significant trend between the inefficiency of wind-forced mixing in raising the mixed layer potential energy and the depth of the pycnocline. In both pilot studies, the cool, saline core of the meanderlike structures were characterized by a shallow pycnocline that acted to impede the surface-generated turbulence from penetrating to middepths (>40 m). Near-surface (<200 m) currents were found to be well explained (80%) by the geopotential anomalies induced by the sloping isopycnals.

The dynamics governing the formation, maintenance, and modification of these complicated features are not completely understood. The importance of cyclostrophic contributions and the distribution of relative vorticity are examples of important dynamical processes that can be resolved only by observations densely sampled both in time and space. A description of the microstructure observations from July 1988 and the analysis presented here will attempt to address some of the fundamental questions related to the structure and dynamics of these upwelled filaments. In particular, the following analysis evaluates a full momentum equation for two orientations corresponding to across-filament and along-filament coordinates. Estimates are made of the ageostrophic contributions, with attempts to determine their significance and the resulting degree of geostrophy. Estimates of the relative vorticity reveal considerable spatial and temporal variability.

[1]Now at Science Applications International Corporation, Bellevue, Washington.

Paper number 91JC00944.
0148-0227/91/91JC-00944$05.00

Typical momentum analyses from current meter and hydrographic observations compare estimates of two or three terms in the momentum equations [*Flament et al.*, 1985; *Huyer and Kosro*, 1987; *McWilliams*, 1976; *Nishida and White*, 1982; *Fofonoff and Hall*, 1983]. A high correlation between the Coriolis acceleration (i.e., fU) and the corresponding pressure gradient $[-1/\rho_0 \partial P/\partial y]$ is often assumed to be sufficient in determining the degree of geostrophy. Ageostrophic contributions (i.e., $\partial V/\partial t$ and $U\partial V/\partial x$) are often omitted because they are assumed to be small and are typically difficult to measure and require repeated observations. Although they are typically smaller than the two "geostrophic" contributions, ageostrophic terms may contribute significantly to the momentum balance. To determine the degree of geostrophy, each term in the momentum equations should be estimated. Only when it has been established that the ageostrophic terms are in fact insignificant can it be stated that the flow is geostrophic.

Previous studies in the area [*Flament et al.*, 1985; *Kosro and Huyer*, 1986; *Huyer and Kosro*, 1987; *Strub et al.*, 1987; *Moum et al.*, 1988; *Dewey and Moum*, 1990] find reasonable correlations between geostrophic and measured velocities, but synopticity and poor temporal resolution give no indication of the magnitude or the net contribution from ageostrophic dynamics. In the following analysis, the data collected along the central "D" line of the hydrographic survey grid [*Huyer et al.*, this issue] will be used to estimate seven terms in the meridional momentum equation.

ADCP observations, both shipboard and moored, are used to estimate the relative vorticity at two locations. Temporal changes, tilting and stretching of vorticity are also estimated in a limited vorticity analysis. Advection of relative vorticity is found to result in regions within the filament of both upwelling and downwelling.

The finely spaced sampling provided by the microstructure profiler reveals an asymmetric structure in the near-surface temperature and salinity distributions that can be explained by cross-frontal exchange. *Strub et al.* [this issue] summarize the complicated water mass structures found in the surface layers across a variety of upwelled filaments and identify possible source regions for the water masses. Steep isopycnal slopes in the frontal region force cross-frontal flow to have vertical components of velocity. This cross-frontal exchange stirs together considerably different water masses. As part of the momentum analysis, the mean vertical velocity structure within the filament is estimated, and the implied divergences and convergences provide a possible explanation for the observed temperature-salinity structure.

The microstructure measurements were collected along a single meridional survey line (D line). The filament bisecting the D line in July 1988 underwent a considerable reorientation between two stable and almost perpendicular aligned phases. During the first phase (phase 1, July 2–16, 1988; Figure 1*a*) the filament axis (as determined by the maximum ADCP velocity vectors) crossed the D line at nearly right angles. After the reorientation (which occurred during strong northerly winds between July 16 and 19), the filament axis was directed southward, crossing the D line at approximately 30° (phase 2, July 20–23, 1988; Figure 1*b*). Microstructure measurements were made during both filament phases.

2. Data

A total of 12 RSVP and 26 shipboard ADCP sections were collected on the R/V *Wecoma* during July 1988. In addition, four current meter moorings were deployed between June 22 and July 23, 1988, 2 km east of the D line, centered about the core of the filament. Two of the moorings were equipped with upward-projecting ADCPs measuring currents in the upper 110 m.

The RSVP system provides vertical profiles of temperature T, salinity S, derived density anomaly σ_t, and the rate of viscous dissipation of turbulent kinetic energy (ε) [*Caldwell et al.*, 1985]. Horizontal profile separation ranged between 0.6 and 1.5 km, with maximum profile depths of 250–160 m, both dependent on the ship speed (1.2–2.5 m s^{-1}). RSVP data were collected during the northward heading transects only, while steaming into the prevailing winds. The shipboard 300-kHz ADCP data consist of 15-min average profiles of U and V in 4-m vertical bins over the depth range 15–250 m. Shipboard ADCP data were recorded while steaming both northward and southward along the D line.

RSVP temperature, salinity, and σ_t data were averaged into profiles with vertical spacing of 2.5 m and horizontal spacing of 1.8 km. The shipboard ADCP data and the RSVP dissipation rate (ε) measurements were averaged into profiles with vertical and horizontal spacing of 5.0 m and 1.8 km, respectively. Continuous sampling along the D line resulted in repeated transects of RSVP data approximately every 2 days and in almost daily ADCP transects (sampled while heading both northward and southward). A total of 12 RSVP and 24 ADCP transects across the filament were collected during the 21-day cruise. These uniformly spaced, gridded data ($U(y, z_5, t_2)$, $V(y, z_5, t_2)$, $T(y, z_{2.5}, t_1)$, $S(y, z_{2.5}, t_1)$, $\sigma_t(y, z_{2.5}, t_1)$, and $\varepsilon(y, z_5, t_1)$) are used in the following analysis to estimate terms in the meridional momentum equation (t_1 indicates RSVP data collected while heading northward only, a total of 12 transects, and t_2 indicates ADCP data collected while heading both northward and southward for a total of 26 transects; $z_{2.5}$ indicates data averaged into vertical bins of 2.5 m (T, S, σ_t), and z_5 indicates 5-m bins (U, V, ε)).

Four current meter moorings were deployed approximately 2 km east of, and parallel to, the D line. Three of these moorings contained upward-projecting 300-kHz ADCPs. Two ADCP moorings, referred to as D2 (latitude 38.1873, longitude 125.0442) and D3 (latitude 37.8323, longitude 124.7781), sampled the upper 110 m (15 to 110 m depths). The moored ADCP data considered in the following analyses consists of 10-min-averaged profiles with 4-m vertical bins. Both shipboard and moored ADCP velocity components have been rotated 30° counterclockwise into "along" (V) and "across" (U) components relative to the hydrographic survey grid.

Errors in the ADCP measurements come from a number of sources [*Kosro*, 1985]. The three most significant sources of error are the near-random fluctuations in the velocity estimates between individual acoustic transmissions caused by varying levels in the acoustic backscatter intensity, variations due to rapid accelerations of the ship (e.g., as a result of surface waves) and errors in the estimated mean ship velocity. The moored data are subject to only the first of these errors. Temporal averaging of consecutive profiles reduces the errors caused by backscatter intensity fluctua-

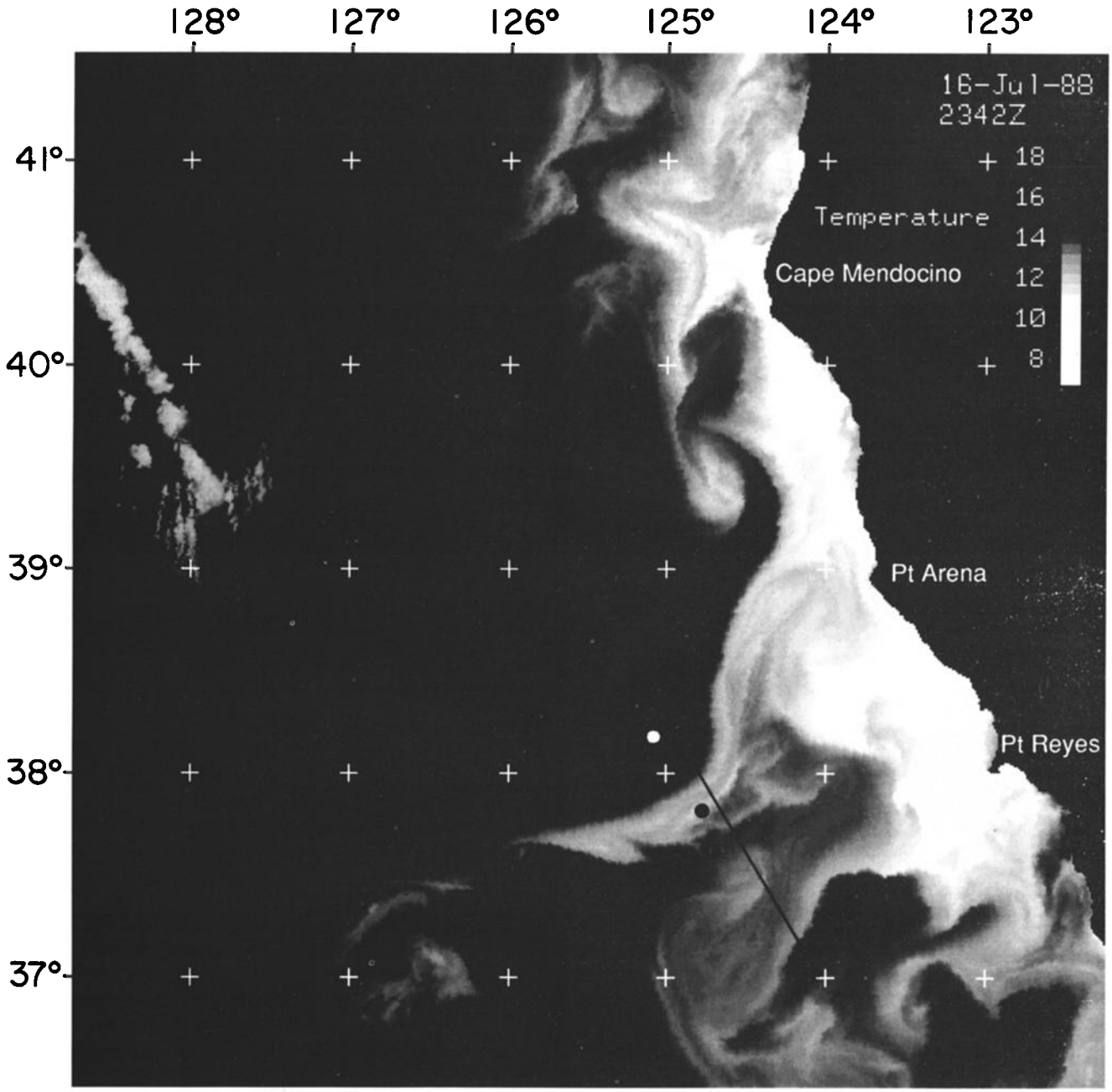

Fig. 1*a*. Advanced very high resolution radiometer (AVHRR) satellite image taken on July 16, 1988, showing the sea surface temperature gradients east of the California coast. The cooler, upwelled water is represented by the lighter shading. The central D line along which the microstructure data were collected is shown, at an angle of 30° from north to south. The maximum current vectors associated with the offshore flow of the filament crossed the D line at right angles for a period of nearly two weeks (July 2–16, 1988). Also shown are the two ADCP mooring locations, D2 to the north and D3 to the south.

tions and waves. Errors in the ship velocity are minimized by careful examination of the navigation data. For this study, LORAN-C navigation was used, lane jumping being the largest source of navigation error. Verification with periodic GPS coverage provided a cross-reference which indicated no major errors or "jumps" had permeated through the analysis. Uncertainty in the 15-min-averaged shipboard ADCP velocities is estimated to be ± 8 cm s^{-1}. Uncertainty in the 10-min-averaged moored ADCP velocities is estimated to be ± 5 cm s^{-1}.

Tidal analysis of the moored ADCP data, using the programs of *Foreman* [1978], indicates significant signal in the semidiurnal M_2 tides. Tidal (M_2) ellipses were aligned in the alongshore (D line) direction with major and minor axes of approximately 9 and 5 cm s^{-1} respectively. This was the only tidal component with associated velocity vectors larger than the estimated uncertainty in the ADCP measurements. The precession of the M_2 tidal vector was clockwise, with a slight phase shift in latitude, the southern mooring (D3) leading the northern (D2) by approximately 30° in the surface values (over a separation of 46 km). This phase shift decreased with depth. The results of the tidal analysis agree with the findings of *Munk et al.*, [1970].

Local accelerations (i.e., $\partial V/\partial t$) have been calculated by

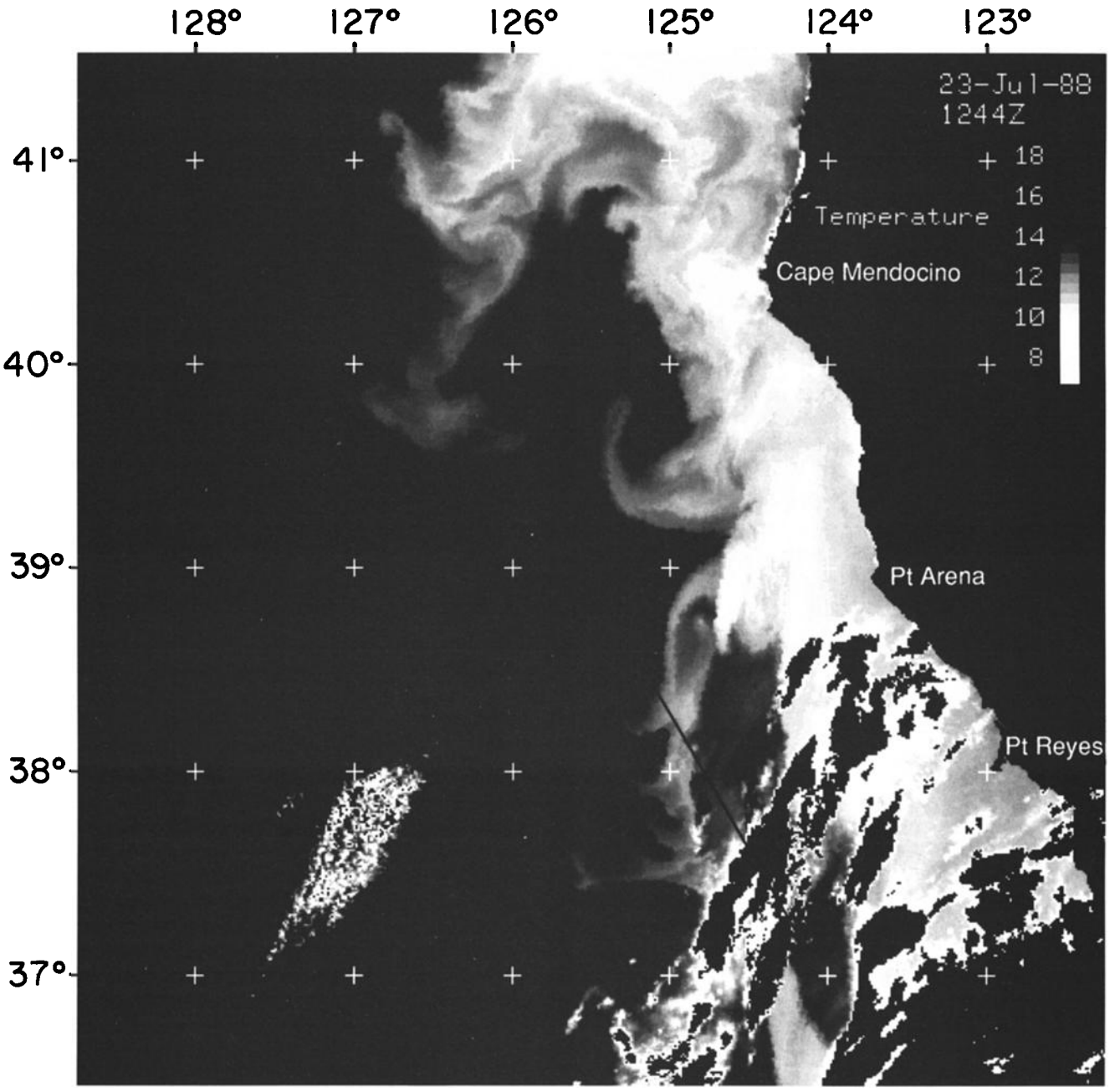

Fig. 1*b*. AVHRR satellite image taken on July 23, 1988, showing the sea surface temperature gradients east of the California coast. The cooler, upwelled water is represented by the light shading. The central D line along which the microstructure data were collected is shown at an angle of 30° from north to south. During this orientation, the current at the D line is due south (July 19–23, 1988).

taking first differences between consecutive transects of the shipboard ADCP velocity estimates (Appendix A). The M_2 tidal component of the flow was removed from the shipboard ADCP before the differencing in order to reduce the effects of aliasing and tidal accelerations. This was accomplished by linear extrapolation of the tidal ellipses along the entire D line. The local tidal vectors (both in time and space) were then predicted and subtracted from the ship ADCP observations. Maximum tidal velocities were of the order of 10 cm s^{-1}, with approximate uncertainties of ± 5 cm s^{-1}. Had these components not been removed, tidal accelerations as large as one-fifth the Coriolis acceleration would have contaminated the local acceleration estimates. Apart from a regional tidal model [*Foreman and Freeland*, 1991], the authors are unaware of other attempts to remove tides from shipboard ADCP data.

The multiple transects of microstructure and shipboard ADCP measurements represent a time series of the across-filament structure. The measurements indicate two reasonably stable filament orientations. During phase 1 (July 2–16, 1988) the velocity vectors were approximately perpendicular to the ship tracks (Figure 2*a*). Eight complete RSVP transects, one partial RSVP transect, and 18 shipboard ADCP transects were made across the filament during this phase. On or about July 18 the filament underwent a rapid, barotropic reorientation. During the second phase (July

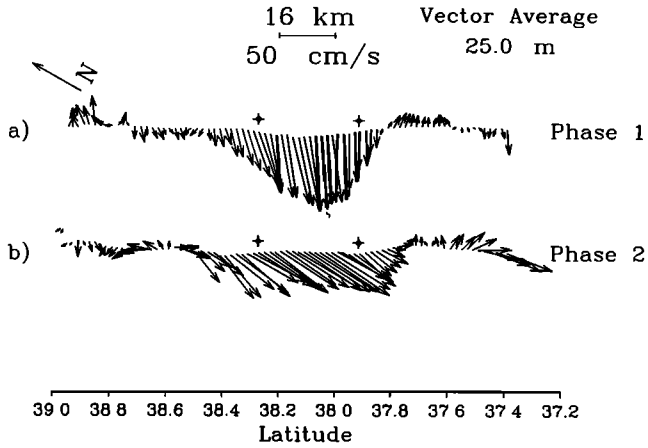

Fig. 2. Average velocity vectors from the shipboard ADCP, for the periods (*a*) July 2–16 and (*b*) July 20–23, 1988. The ship track (D line) is oriented at 30° from true north. Approximately 18 transects (not all were complete from end to end) were averaged during Phase 1, and six transects were averaged for Phase 2. The locations of the two ADCP moorings are also shown, displaced approximately 4 km to the northeast of the D line. The latitude scale for all figures is the projection of latitude onto the D line, with 1° ≈ 128 km.

20–23, 1988) the maximum velocity vectors associated with the filament were due south (Figure 2*b*). Three RSVP and six ADCP transects were made during the phase 2 orientation. Although the current vectors during phase 2 are not exactly "along" the ship track, the 60° veering of the current will be considered sufficient to investigate the relative importance of meridional geostrophy between the two phases.

Shown in Figures 3*a* and 3*b* are the temperature, salinity, σ_t, and U (perpendicular to the D line) values at 25 and 125 m depth, respectively, during phase 1. The surface (25 m) structure is less stationary than the deeper (125 m) structure. The northern surface signature of the filament gradually progresses southward during the 2-week observation period (July 2–16, 1988). Shown in Figures 4*a* and 4*b* are the temperature, salinity, σ_t, and U values at 25 and 125 m depth for phase 2.

Temporal averages of temperature, salinity, σ_t, U, and V for Phase 1 are shown in Figure 5. The averages for Phase 1 were calculated from nine RSVP (northward heading only) and eighteen ADCP (northward and southward heading) transects. Figure 6 shows the same fields for Phase 2 (averaged from three RSVP and six ADCP transects, respectively). The average sections for Phase 2 have larger variances, as they are constructed from fewer observations. The effects of small-scale fluctuations, such as internal waves, have not been as greatly reduced in the phase 2 averages.

During the entire period of the microstructure cruise the location of the two ADCP current meter moorings bounded the core of the velocity jet (Figure 2). The northern mooring (D2) remained within the negative relative vorticity, and the southern mooring (D3) remained within the positive relative vorticity. The ship tracks (along the D line) passed the

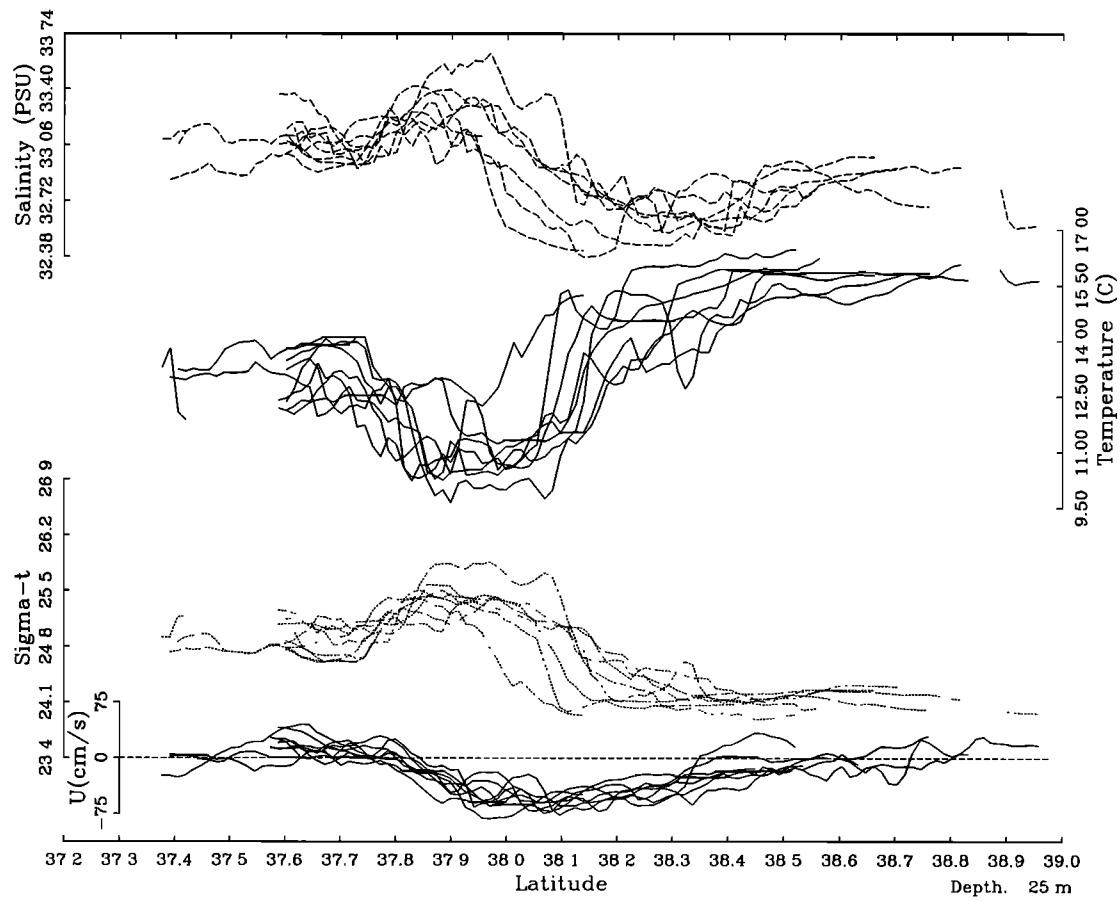

Fig. 3*a*

Fig. 3. Temperature, salinity, σ_t, and U at (*a*) 25 m and (*b*) 125 m depth from each transect representing phase 1 (July 2–16, 1988). Maximum variability is near the surface and the northern signature of the front. With depth, variability is reduced, and the front becomes more "one sided."

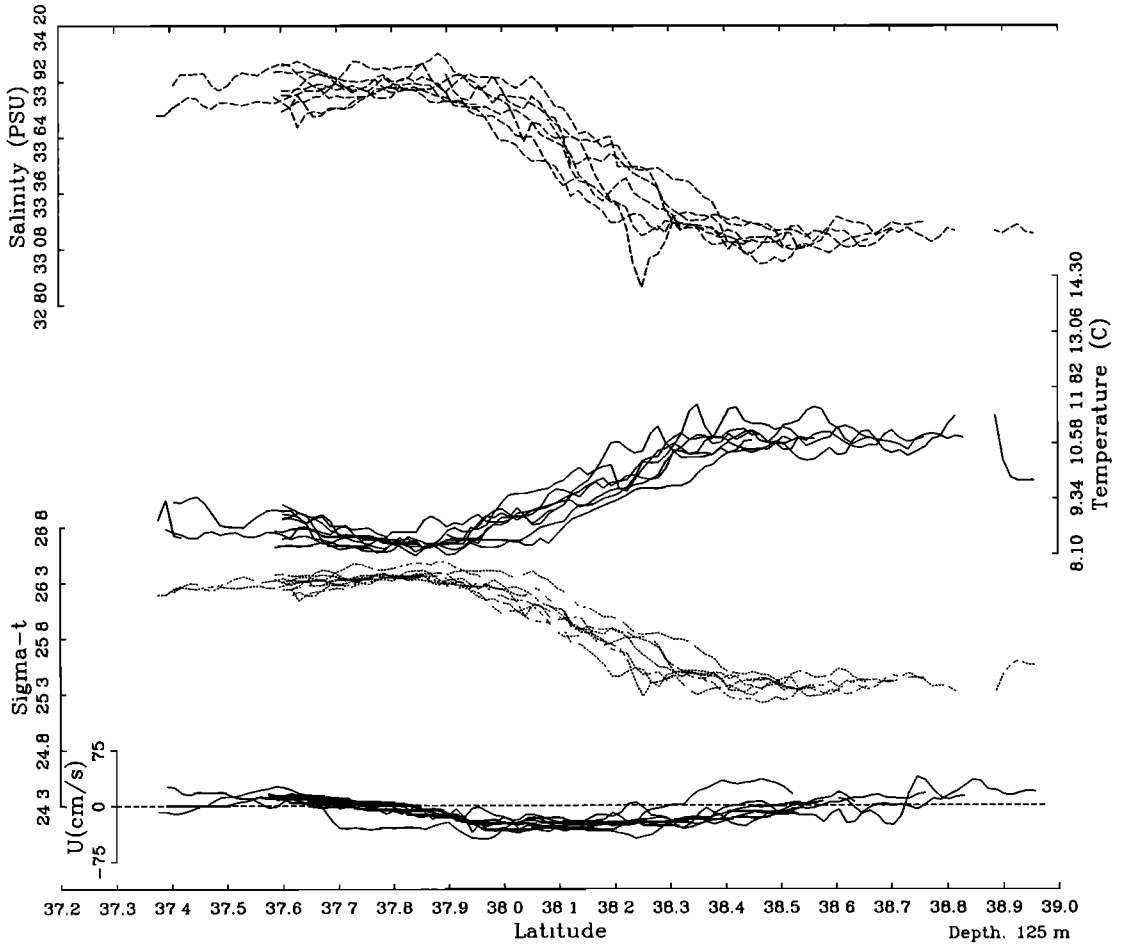

Fig. 3*b*

moorings at between 2 and 8 km to the southwest. This combination of ship and moored ADCP data allows an analysis of vorticity at two locations either side of the jet.

In the following analyses, vertical gradients are estimated by differencing the gridded data over 10 m. Although differencing underestimates a differential, we make no attempt to correct for this underestimate in our calculations. The RSVP data (T, S, σ_t, and ε) are independent at vertical length scales shorter than 10 m, while our ADCP estimates of U and V are independent at separations of 16 m. This is a result of the acoustic pulse length, the gating and filtering used in processing the ADCP data. As a result, 12-m (three bin) separations in the original ADCP data are nearly independent, and 16-m (four bin) separations are completely independent.

3. Momentum Balance

The primitive zonal and meridional momentum equations can be written [*Pedlosky*, 1978],

$$\frac{\partial U}{\partial t} + U\frac{\partial U}{\partial x} + V\frac{\partial U}{\partial y} + W\frac{\partial U}{\partial z} - fV = -\frac{1}{\rho_0}\frac{\partial P}{\partial x} + \frac{1}{\rho_0}\nabla\cdot\tau_{xi} + \nu\nabla^2 U, \qquad (1a)$$

$$\frac{\partial V}{\partial t} + U\frac{\partial V}{\partial x} + V\frac{\partial V}{\partial y} + W\frac{\partial V}{\partial z} + fU = -\frac{1}{\rho_0}\frac{\partial P}{\partial y} + \frac{1}{\rho_0}\nabla\cdot\tau_{yi} + \nu\nabla^2 V, \qquad (1b)$$

where the terms represent local acceleration, rate of change of momentum due to advection, Coriolis acceleration, pressure gradient, submesoscale flux divergence (where the stress for each component n is $\tau_{ni} = (\tau_{nx}, \tau_{ny}, \tau_{nz})$), and viscous diffusion. The central two terms for each component represent the well-known geostrophic equations. For this reason the terms fU and $(-1/\rho_0)(\partial P/\partial y)$ will be referred to as the geostrophic terms, without implying that the flow is purely "geostrophic." Data collected along the "north-south" D line can be used to estimate terms in the meridional momentum equations (1*b*) only. Apart from the viscous term, which is very small and can be omitted from the analysis without consequence, we have been able to estimate the remaining seven terms in (1*b*).

Details on the estimation of each term in the meridional momentum equation (1*b*) from the measured quantities are presented in Appendix A. The technical details of the calculations have been separated from the present discussion of dynamics in order to keep the focus on the physics.

The dominant terms in (1*b*) are the two geostrophic terms.

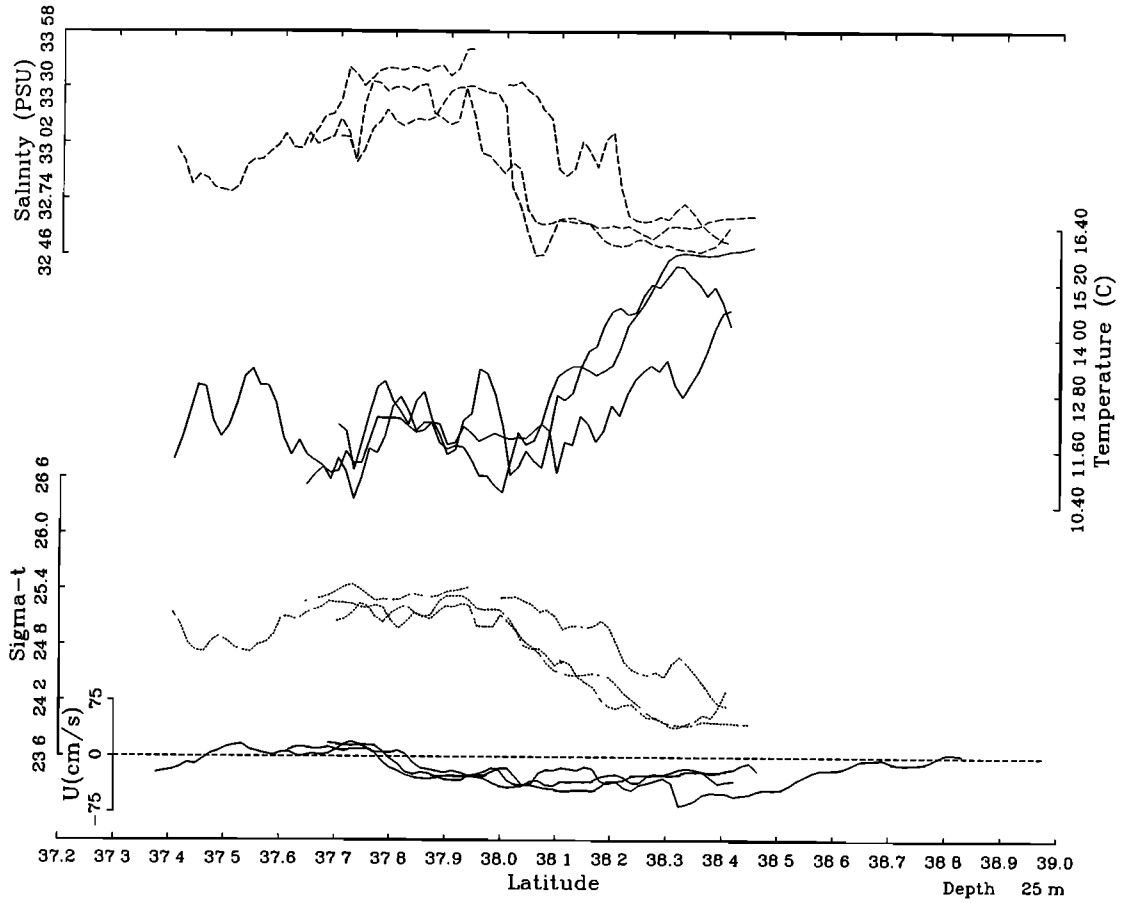

Fig. 4a

Fig. 4. Temperature, salinity, σ_t and U at (*a*) 25 m and (*b*) 125 m depth from each transect representing Phase 2 (July 20–23, 1988). Maximum variability is near the surface and the northern signature of the front. With depth variability is reduced, and the front becomes more "one-sided."

The Coriolis term is simply the zonal velocity U as measured by the ADCP, multiplied by the local mean Coriolis component of rotation $f(=8.98 \times 10^{-5}\ \mathrm{s}^{-1})$. The meridional pressure gradient $-(1/\rho_0)\partial P/\partial y$ was calculated from horizontal differences in the geopotential anomaly $\int_0^p \delta dp$, where δ is the specific volume anomaly determined from RSVP profiles of T, S, and p. A level (pressure) of known motion was taken to be 150 m, the geopotential anomaly gradient set equal to the ADCP-measured Coriolis term (fU) at this depth. Measurement errors in ADCP velocity estimates increase with depth below 150 m. By setting these terms equal at 150 m depth, we recover only differences in measured and geostrophic shear between 150 m and the surface and therefore do not recover all of the ageostrophy in the flow. Velocities within the jet are still considerable at 150 m ($\sim$20–30 cm s^{-1}), and ageostrophy remains unresolved.

Shown in Figure 7*a* are the mean geostrophic terms for phase 1 (July 2–16), $\langle fU \rangle$ (solid) and $\langle -(1/\rho_0)\partial P/\partial y \rangle$ (dashed), each scaled by $100/f$, so the values are equivalent to zonal flow in centimeters per second. The angle brackets represent a temporal average from consecutive transects. The geostrophic residual is shown in Figure 7*b*. Each mean value in the momentum analysis has also been depth averaged between 20 and 30 m. Confidence intervals (95%) have been estimated using a bootstrap (Monte Carlo) technique [*Efron*, 1987]. The residual is not significantly different from zero at the 95% confidence level (summed confidence intervals) along the entire D line.

A linear regression between the two geostrophic terms (Figure 8) indicates an offset of -6.3 (cm s^{-1}), a regression coefficient of 1.03, and a correlation coefficient of $r = 0.94$ with a 95% bootstrap confidence interval of 0.02. (The 95% confidence interval for each coefficient is indicated in Figure 8.) From the combined nine transects, a total of 89 independent observations are estimated, by dividing the total record by the observed integral length scale as determined from the autocorrelation. Therefore based on the number of independent observations, a correlation $|r| > 0.21$ is significantly different from zero at the 95% confidence level [*Bendat and Piersol*, 1986]. The residual difference [*Priestley*, 1989] between the geostrophic terms (Figure 7*b*) indicates that $(\sigma^2_{fU} - \sigma^2_{\mathrm{res}})/\sigma^2_{fU} = 89\%$ of the observed variance in the Coriolis acceleration σ^2_{fU} is explained by the geopotential anomaly.

Without estimating ageostrophic contributions, one might conclude that the residual of the geostrophic terms, with a variance of $\sigma^2_{\mathrm{res}} \simeq 66\ \mathrm{cm}^2\ \mathrm{s}^{-2}$, represents the full contribution from ageostrophic dynamics, plus any noise in the two geostrophic estimates, representing only 5.6% of the accumulated variance. It is possible, on the other hand, that local accelerations ($\partial V/\partial t$) are balanced entirely by cyclostrophic adjustments ($U\partial V/\partial x$, $V\partial V/\partial y$). In such a case, determining

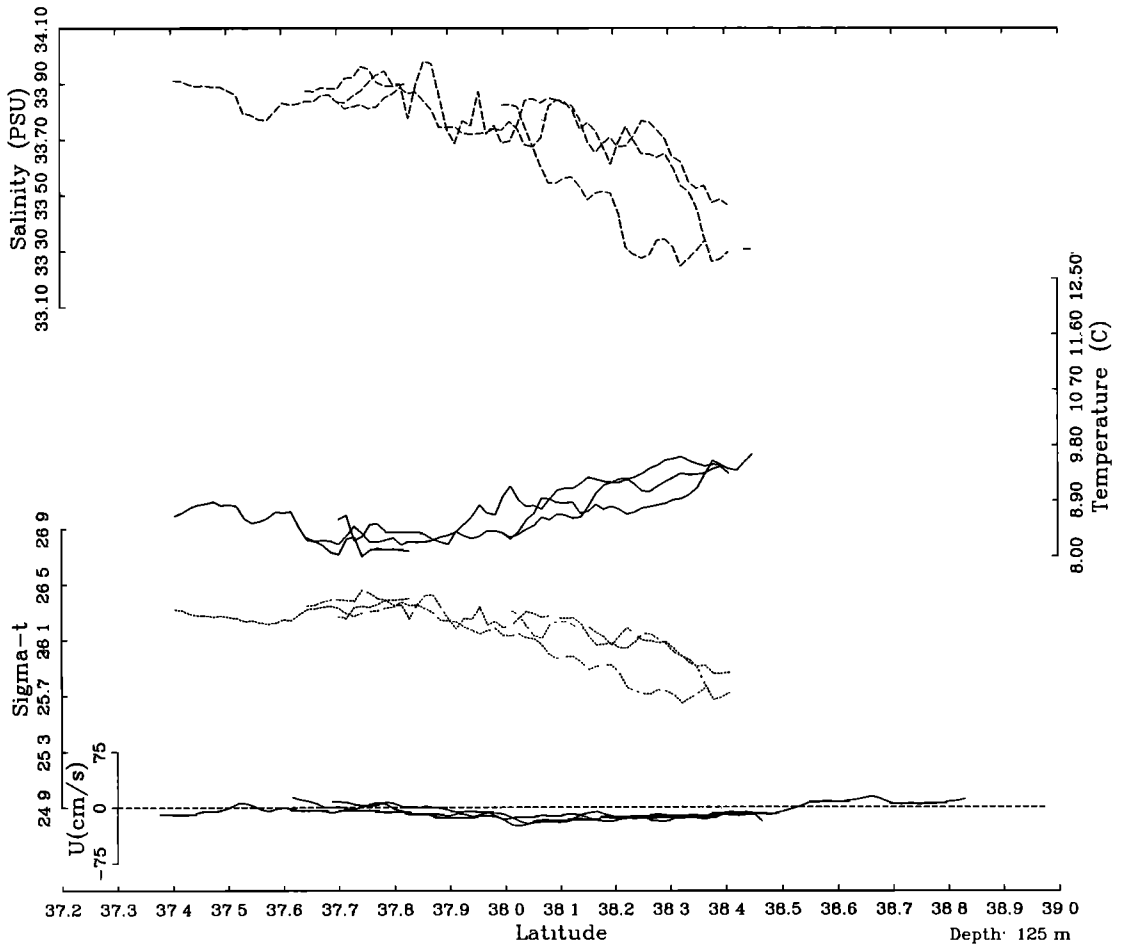

Fig. 4*b*

a balance between fU and $-(1/\rho_0)\partial P/\partial y$ would be insufficient for assessing the geostrophic character of the flow. A geostrophic flow must have insignificant ageostrophic contributions, regardless of the correlation between the two "geostrophic" terms. Any conclusion on the degree of geostrophy must include an evaluation of the ageostrophic terms.

During phase 1, mean current vectors (Figure 2*a*) were perpendicular to the D line. The mean density section therefore resolved the maximum pressure gradient and thus represents a good test for geostrophy. Simple scaling arguments predict [*Pond and Pickard*, 1978] a maximum degree of geostrophy across a strong mean current. Similarly, geostrophy is not expected to be as dominant in the momentum component aligned parallel to the axis of a strong current. Although a very high degree of correlation is found between the geostrophic terms, there is no a priori reason to expect each ageostrophic term to be negligible, although we may expect them to have a small net contribution to the balance since the unexplained residual is already small. During phase 2, mean current vectors crossed the D line much more obliquely, at 30° from meridional (Figure 2*b*). These observations provide a reasonable test of the hypothesis that the ageostrophic components of the momentum equation will have increased importance along the axis of the "jet."

During phase 2, only 76% of the observed variance in the Coriolis acceleration fU is explained by the meridional gradient of the geopotential anomaly (Figure 9). The linear regression between the two geostrophic terms (Figure 10) indicates a correlation of $r = 0.87$, with a 95% bootstrap confidence interval of 0.05. From the combined three transects of phase 2, a total of 24 independent observations are estimated, and therefore a correlation $|r| > 0.41$ is significantly different from zero at the 95% confidence level. The linear regression between the two geostrophic terms for phase 2 (Figure 10) indicates an offset of 0.33 (cm s^{-1}) and a regression coefficient of 1.05. Again, if the geostrophic residual, with a variance of $\sigma^2_{res} \simeq 76$ cm^2 s^{-2}, represents all the ageostrophic dynamics plus any noise in the geostrophic terms, the ageostrophic variance accounts for a maximum of 13% of the total meridional momentum variance.

The difference between the "geostrophic" correlation coefficients for phase 1 and phase 2 is $\Delta r = 0.07$ with a 95% uncertainty of ± 0.05. The difference is significantly different from zero, and the correlations are therefore significantly different at the 95% confidence level. Although the correlation for phase 2 suggests a lower degree of geostrophy, the confidence intervals are larger owing to the much lower number of observations (three versus nine RSVP transects, and 24 versus 89 independent "observations"). At this stage of the analysis it is not clear whether a true decrease in the meridional geostrophy has been revealed, and in particular, what physics may be causing the ageostrophy, or whether

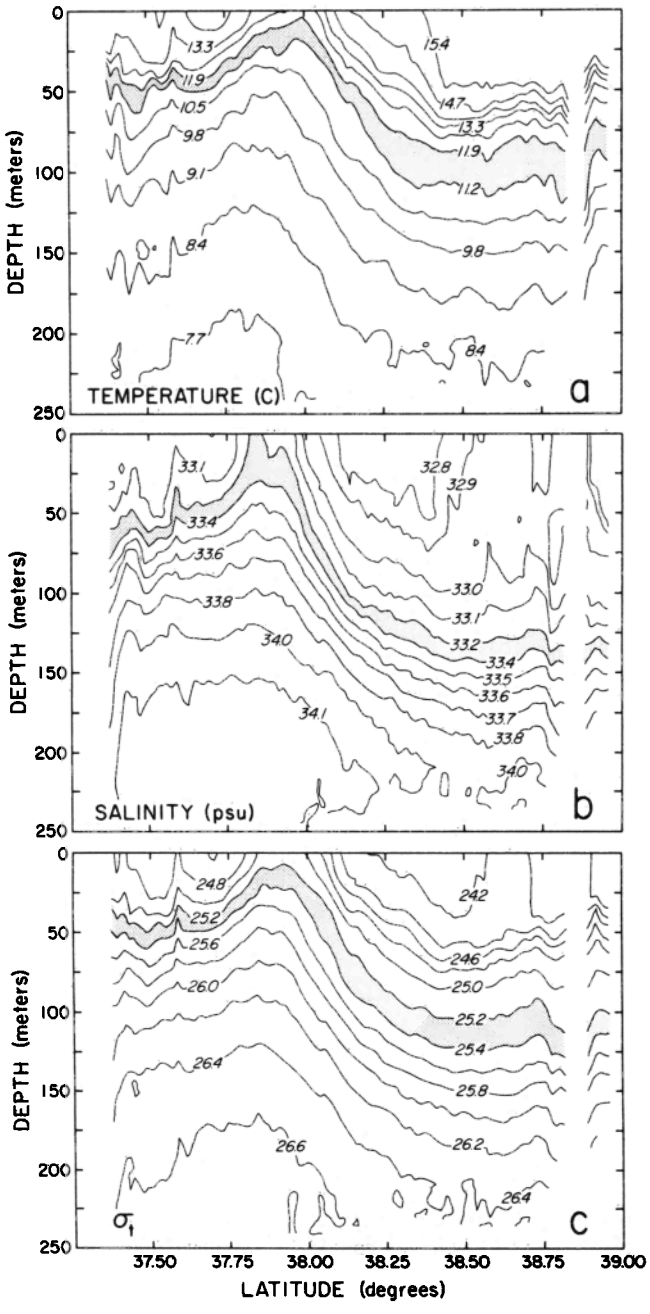

Fig. 5. Contour plots of the average (*a*) temperature, (*b*) salinity, and (*c*) σ_t structure as revealed by RSVP measurements and of the average ADCP velocity structure (*d*) *U* and (*e*) *V* along the D line for July 2–17, 1988. The data in Figures 5*a*, 5*b*, and 5*c* have been averaged onto a fixed latitude grid with approximately 1.8 km by 2.5 km resolution in the horizontal and vertical directions, respectively. A total of nine RSVP transects make up the averages, with fewer samples near the northern, southern, and deeper boundaries. Maximum isopleth displacement across the front is ~100 m. The data in Figures 5*d* and 5*e* have been averaged onto a fixed latitude grid with approximately 1.8 km by 5 m resolution in the horizontal and vertical directions, respectively. The coordinate system is rotated 30° from true north; *U* is therefore perpendicular to the D line and *V* is parallel to the *D* line. A total of 18 ADCP transects make up the averages, with fewer samples near the northern, southern, and deeper boundaries.

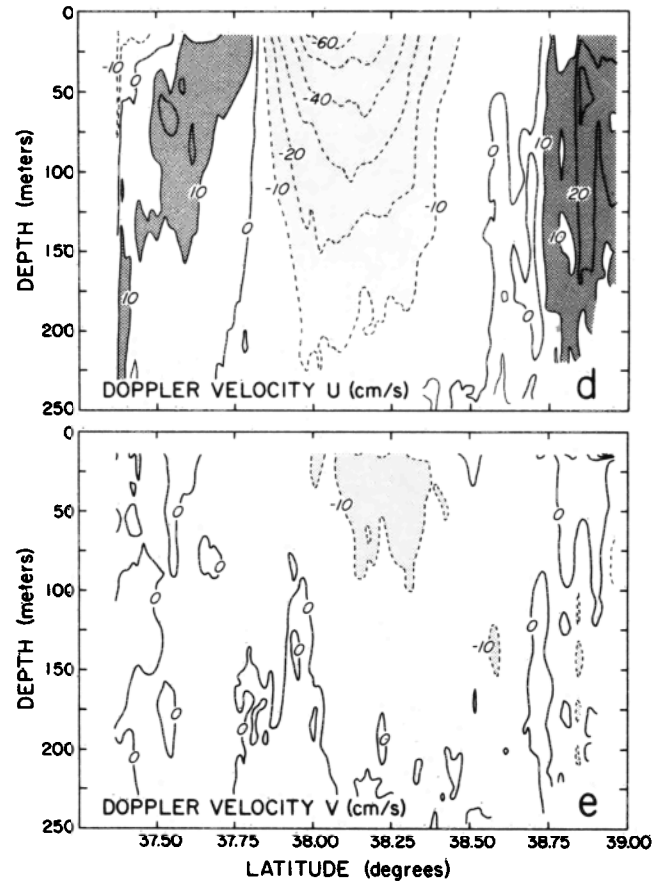

Fig. 5. (continued)

there is simply a reduced signal to noise level during phase 2. Estimation of the ageostrophic terms in (1*b*) will attempt to address these points and determine whether true balances have been obtained. Also, a momentum balance from three consecutive transects during phase 1 will provide some indication of the variability due to the decrease in the number of observations and therefore the apparent "signal to noise" during phase 2. Since the momentum equations are always obeyed, the goal is to show that our observations and calculations represent significant estimates of both the geostrophic and ageostrophic contributions.

The details of estimating each ageostrophic term detract somewhat from the present discussion, and therefore have been relegated to Appendix A. In arriving at an estimate of the mean vertical advection of meridional momentum, $W(\partial V/\partial z)$, a calculation for mean vertical velocities W is presented in Appendix B.

During phase 1, no ageostrophic contribution was significantly different from zero at the 95% confidence level. Zonal advection south of the filament core was the largest ageostrophic component during phase 1, with a magnitude (scaled by 100/*f*) of $(U/f)\partial V/\partial x \simeq 10$ cm s^{-1}. Despite this relatively large mean contribution, considerable variability in $U\partial V/\partial x$ results in a large confidence interval, rendering the mean insignificantly (at 95%) different from zero. During phase 2, both the acceleration ($\partial V/\partial t$) and meridional advection ($V\partial V/\partial y$) terms indicate regions significantly different from zero, with scaled magnitudes as large as 5 and 10 cm s^{-1}, respectively.

After adding the estimated ageostrophic terms to the geostrophic residual, we can reevaluate the total level of geostrophy of the meridional momentum balances. During phase 1 the mean pressure gradient $-(1/\rho_0)\partial P/\partial y$ explained

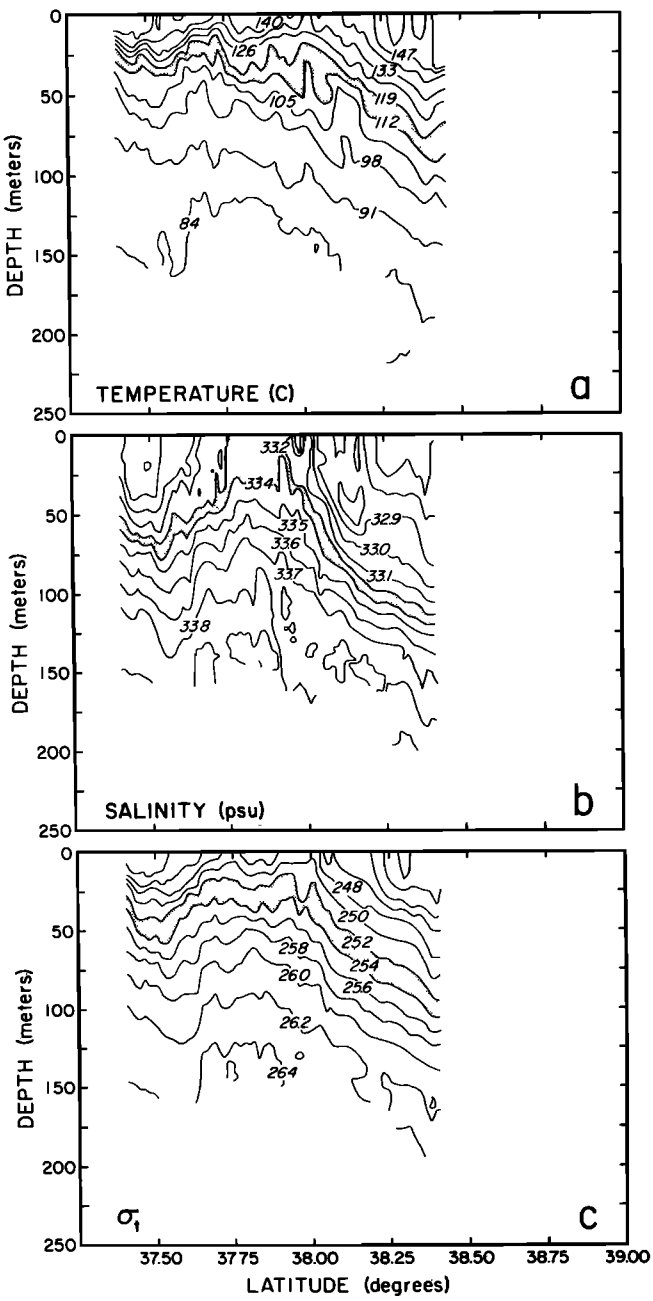

Fig. 6. Contour plots of the average (*a*) temperature, (*b*) salinity, and (*c*) σ_t structure as revealed by the RSVP and of the average ADCP velocity structure (*d*) *U* and (*e*) *V* along the D line for July 20–23, 1988. The data in Figures 6*a*, 6*b*, and 6*c* have been averaged onto a fixed latitude grid with approximately 1.8 km by 2.5 m resolution in the horizontal and vertical directions, respectively. A total of three RSVP transects make up the averages, with fewer samples near the northern, southern, and deeper boundaries. The data in Figures 6*d* and 6*e* have been averaged onto a fixed latitude grid with approximately 1.8 km by 5 m resolution in the horizontal and vertical directions, respectively, and rotated through 30° into the D line coordinates. A total of six ADCP transects make up the averages, with fewer samples near the northern, southern, and deeper boundaries.

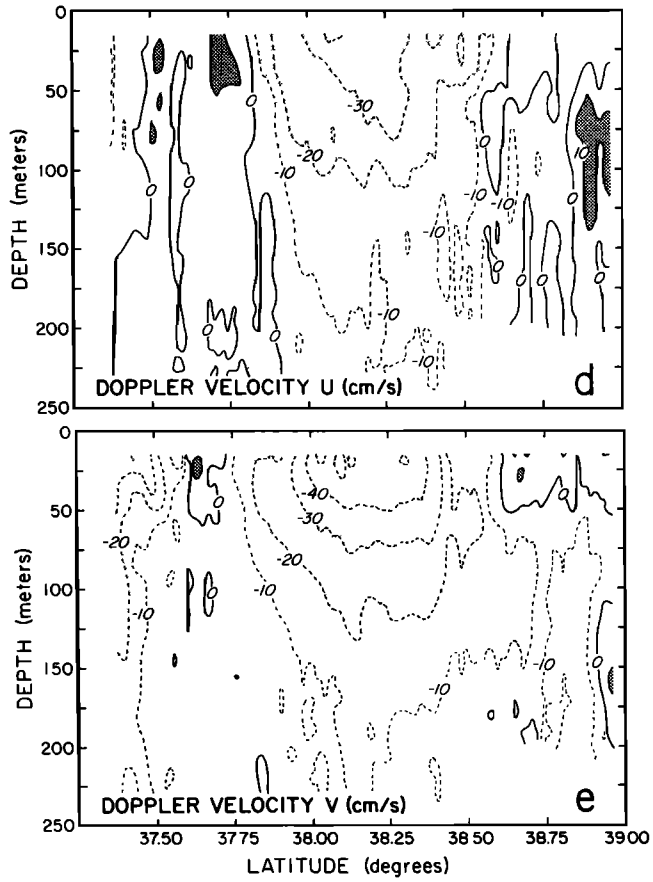

Fig. 6. (continued)

89% of the variance in (fU) and 87% of the variance from all contributions to the meridional momentum equation. Ageostrophic contributions were never significantly different from zero and show little coherent structure. Even the mean zonal advection term ($U\partial V/\partial x$), the largest ageostrophic contribution, was not significantly different from zero. Therefore during phase 1 the zonal or along-filament current was in geostrophic balance to within the accuracy of the present measurements and the observed noise variance.

Phase 2, representing an approximation to across-filament dynamics, indicates a significant decrease in the level of geostrophy. The mean meridional pressure gradient explains 76% of the variance in (fU), and 70% of the variance in the total balance. The ageostrophic components were occasionally significantly different from zero at the 95% level; however, they fail to reduce the relative variance accumulated in the residual, indicating separate regions of coherent increase and decrease in the balance residual. Nonetheless, the mean pressure gradient, the second largest term in the balance, contributes 9% less to the momentum balance during phase 2 than in the perpendicular case represented by phase 1.

In order to estimate the relative change in the signal to noise level during phase 2, introduced by the fewer number of observations, a series of three consecutive transects during phase 1 are analyzed. It will be assumed that noise sources during the two phases are similar and that a change in the signal to noise represents a decrease in the signal. This may not be the case, but our observations provide no indication that the noise (e.g., internal wave displacements of isopycnals) is different between phases 1 and 2. The geostrophic momentum terms for this three-transect phase 1 balance are shown in Figure 11. During this 4-day period (July 10–13) the mean pressure gradient accounts for 88% of the variance in the observed velocity field, and an unchanged

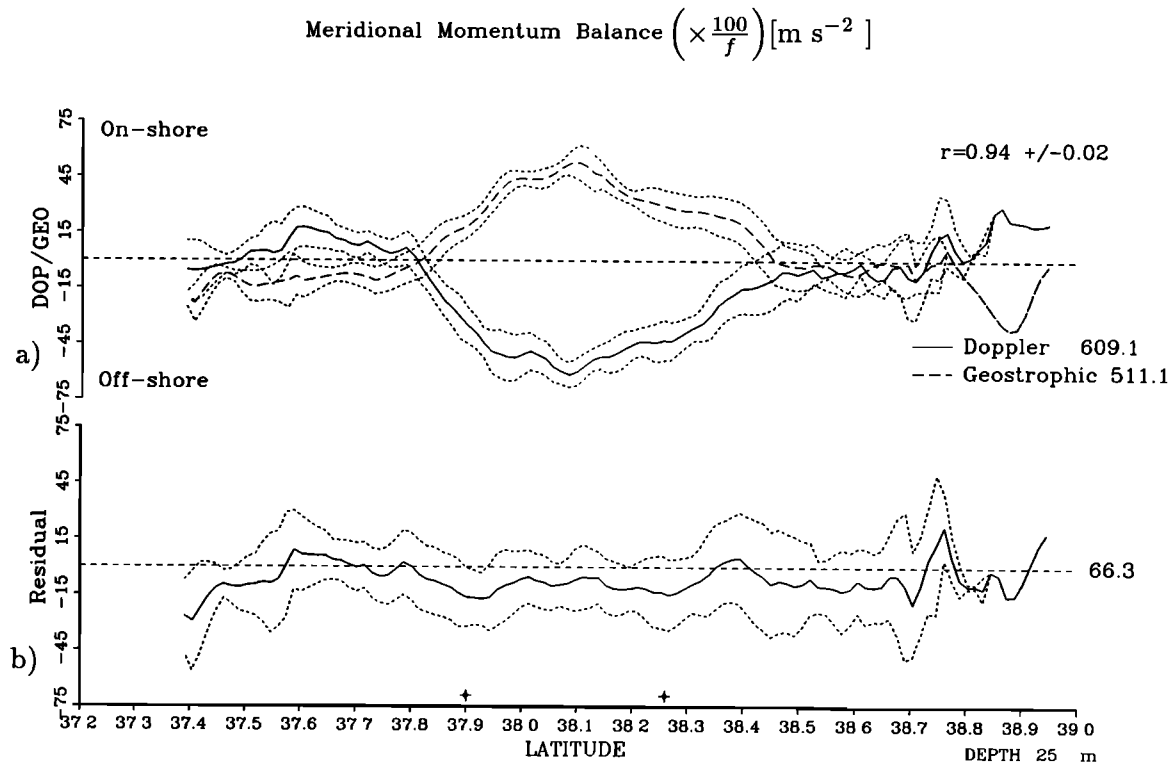

Fig. 7. (*a*) Temporal averages of the ADCP zonal velocity U (solid line) and the negative geostrophic velocity $(1/f\rho_0)\partial P/\partial y$ (longed-line dash) in centimeters per second for the first filament orientation (phase 1), each shown with 95% confidence intervals. A 10-m vertical average has also been applied, centered at a depth of 25 m. A total of 500 bootstrap iterations were performed, with 95% confidence limits calculated from the resulting distributions. The correlation between the observed (ADCP) and the geostrophic currents is $r = 0.94$ with a bootstrap confidence interval (95%) of 0.02. To the right of the labels are the variances of the two series (in cm^2 s^{-2}). (*b*) The "geostrophic" residual in centimeters per second, simply the difference between the series shown in Figure 7*a*. The confidence interval is the sum of the two individual 95% intervals. The variance of the residual is indicated at the right. The two symbols at the bottom indicate the location of the moored ADCPs.

88% of the variance in the total balance. The correlation coefficient between the geostrophic terms is $r = 0.94$ with a 95% confidence interval of 0.02. Based on the number of independent observations (15), a coefficient $|r| > 0.51$ is significantly different from zero at the 95% confidence level. These results are nearly identical to the total balance for phase 1 estimated by including all nine transects. The variances of the estimated ageostrophic components are below the noise levels, and the final residual indicates that ageostrophy does not significantly contribute to the balance. The increased variability in the ageostrophic terms and reduced correlation between the two geostrophic terms for phase 2 is therefore not due to the analysis of fewer observations but likely represents a true decrease in the level of geostrophy.

4. Vorticity Analysis

The location of the ADCP moorings is such that between July 2 and 16 the northern mooring (D2) remained north of the jet core and the southern mooring (D3) remained south of the jet core (Figure 2). Across a uniform jet the relative vorticity changes from positive to negative. The following analysis is intended to reveal the magnitude, structure, and variability of the vorticity field across the observed filament.

The vorticity equation is derived by simply cross differentiating and subtracting the linear momentum equations (1*a*) and (1*b*), thus eliminating the pressure gradient terms. (We have also assumed here that the viscous terms in (1) can be ignored.) After some algebra the vorticity equation can be written,

$$\frac{\partial\zeta}{\partial t} + U\frac{\partial\zeta}{\partial x} + V\frac{\partial\zeta}{\partial y} + W\frac{\partial\zeta}{\partial z} + V\beta\cos(30°) + U\beta\sin(30°) - f\frac{\partial W}{\partial z} - \left(\xi\frac{\partial W}{\partial x} + \eta\frac{\partial W}{\partial y} + \zeta\frac{\partial W}{\partial z}\right) = 0, \quad (2)$$

where the velocity components are in the D line coordinates. (This coordinate transformation results in both components of flow in the D line system contributing to the advection of planetary vorticity, thus the β cos and β sin in (2).) The three-dimensional relative vorticity is given by

$$\zeta = (\xi, \eta, \zeta) = \left(\frac{\partial W}{\partial y} - \frac{\partial V}{\partial z}, \frac{\partial U}{\partial z} - \frac{\partial W}{\partial x}, \frac{\partial V}{\partial x} - \frac{\partial U}{\partial y}\right). \quad (3)$$

Terms in the vorticity equation (2) represent the rate of change of relative vorticity, advection of relative vorticity, advection of planetary vorticity, stretching of planetary vorticity, and tilting and stretching of relative vorticity.

At each mooring location (D2 $\simeq$ 38.27° and D3 $\simeq$ 37.9°) the total relative vorticity ζ was estimated by first differencing ADCP velocity estimates between the mooring and ship track locations and along the ship track. For differences

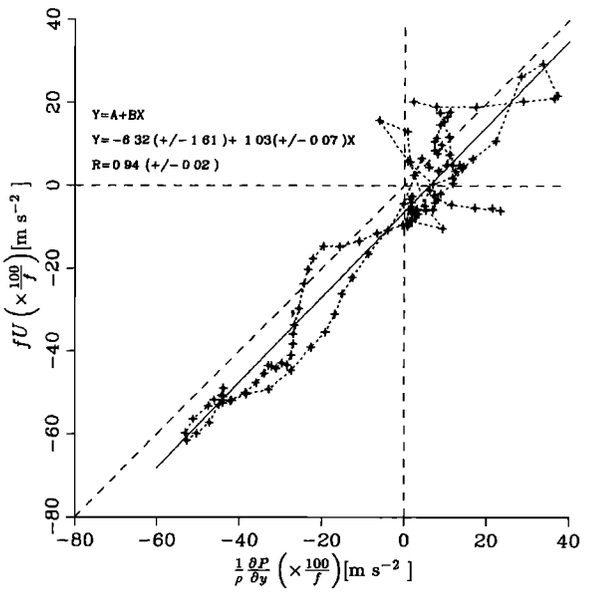

Fig. 8. An linear regression (solid line) between the average ADCP zonal current (U) and the scaled average pressure gradient $(1/f\rho_0)\partial P/\partial y$ during phase 1. The uncertainty for each regression coefficient is 95%.

between the mooring locations and the ship track velocities, the shipboard ADCP data were averaged into 12-km bins and the mooring data were averaged temporally for periods equivalent to the spatial averages based on the ship speed. Both northward and southward transects were used, the ship speed doubling (ranging from 1.2–2.5 m s^{-1} to 4.0–6.0 m s^{-1}) between northward- and southward-heading transects, respectively. The averaging period varied similarly, from ~1.5 hours for the northward (slower) transects to ≤1 hour for the southward (faster) transects.

The zonal gradient in relative vorticity ($\partial\zeta/\partial x$) cannot be estimated from our meridional transects, and $\partial\zeta/\partial y$ can be evaluated only between the two mooring sites, across the jet. Temporal changes can be estimated from the time series of ζ provided by the repeated transects. All other terms are estimated directly from the ADCP-measured U and V velocities and W estimated from the first term in (B4).

Figure 12 shows the relative vorticity at a depth of 25 m for both the northern (D2) and southern (D3) locations (scaled by $1/f$). The large negative value during Julian day 190 (D2, July 8, 1988), $\zeta = -0.95f$, is the result of significant $\partial V/\partial x$ shear between the ship and moored ADCP data at D2. Poor ship navigation is believed to have caused this "error," although there is not discernible reason for rejecting the navigation data used (P. M. Kosro, personal communication, 1990) and the subsequent ship velocity vectors. Nonetheless, this vorticity value is in question. Such large negative vorticities are unlikely, since instabilities in potential vorticity dynamics (proportional to $[1/(f + \zeta)]$) act to diffuse momentum in regions of strong negative vorticity [*Hoskins*, 1974, 1982]. The large positive vorticity during day 188 (D3, July 6) is believed to be real, indicating relative vorticity equal to planetary vorticity.

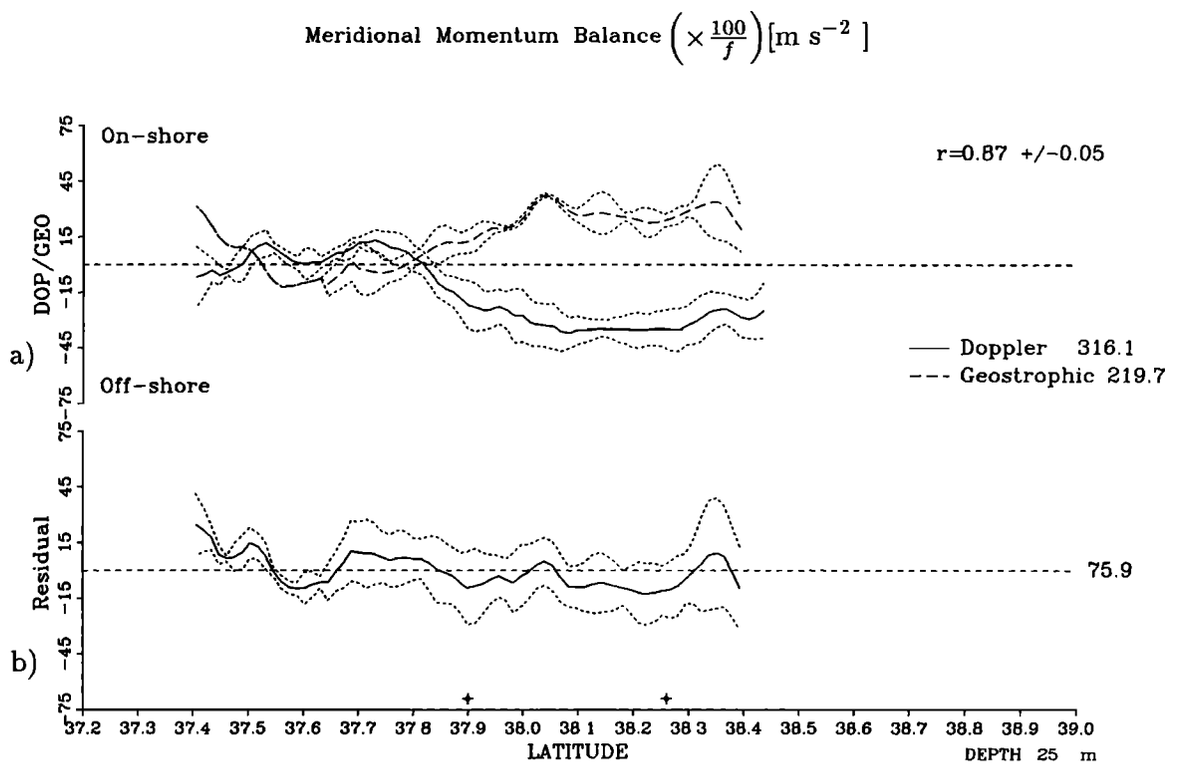

Fig. 9. (*a*) Temporal averages of the ADCP zonal velocity U (solid line) and the negative geostrophic velocity $(1/f\rho_0)\partial P/\partial y$ (long-dashed line) in centimeters per second for phase 2, each shown with 95% confidence intervals. The values have also been vertically averaged over 10 m, centered at a depth of 25 m. The correlation between the observed (ADCP) and the geostrophic currents is $r = 0.87$ with a bootstrap confidence interval (95%) of 0.05. To the right of the labels are the variances of the two series (in cm^2 s^{-2}). (*b*) The "geostrophic" residual in centimeters per second, simply the difference between the series shown in Figure 9*a*. The confidence interval is the sum of the two individual 95% intervals. The variance of the residual is indicated at the right. The two symbols at the bottom indicate the location of the moored ADCPs.

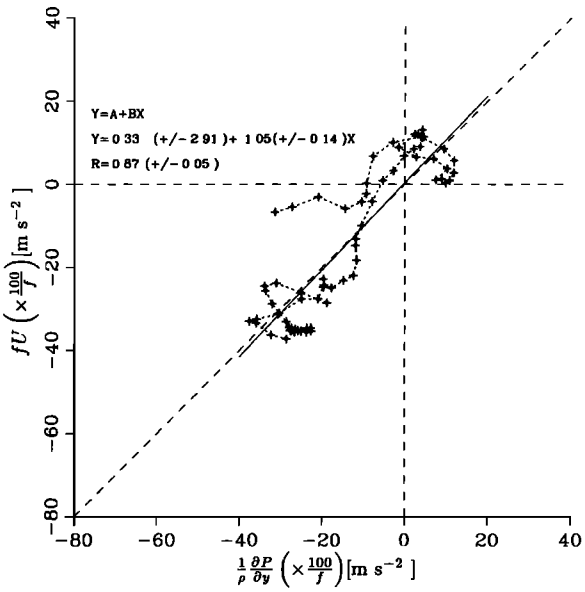

Fig. 10. A linear regression (solid line) between the average ADCP zonal current (U) and the scaled average pressure gradient $(1/f\rho_0)\partial P/\partial y$ during phase 2. The uncertainty for each regression coefficient is 95%.

The northern mooring location is a site of consistent negative relative vorticity and the southern mooring a location of positive vorticity (Figure 12). The time-averaged means for the two periods are also shown (Figure 12) with error bars of 1 standard deviation. The temporal mean relative vorticities are approximately $\langle\zeta\rangle = -0.16f$ and $\langle\zeta\rangle = 0.25f$ for the northern and southern mooring locations, respectively (not including the erroneous low value on Julian day 1990). This assymetry in the shear can be seen in the mean current vectors (Figure 2*a*). Considerable asymmetry was also observed by *Kosro and Huyer* [1986] during a 1982 survey of a similar filament. As was indicated above, instabilities that work preferentially in regions of large negative relative vorticity act to "diffuse" momentum (vorticity), thus spreading the shear and perhaps contributing to the current asymmetry observed [*Hoskins*, 1974; *Haidvogel et al.*, this issue; *Huyer et al.*, this issue].

Not all terms in (2) can be estimated, and a vorticity balance will not be attempted, although the available terms can be compared in a limited vorticity analysis. Shown in Figure 13 are the significant time series and temporal means for four terms in the vorticity equations (scaled by $1/\beta$) at both mooring locations (D2 in Figure 13*a*, D3 in Figure 13*b*) and the residual (plot 5) of the six estimated terms. The dominant terms are the observed temporal changes ($\partial\zeta/\partial t$) (plot 1) and the stretching of planetary vorticity ($f\partial W/\partial z$) (plot 3). Tilting and stretching of relative vorticity (plot 4) contributes significantly only during a 1-day period at location D2 (Figure 13*b*; July 14; Julian day 196). Advection of planetary vorticity is smaller than all other terms by more than 2 orders of magnitude (not shown). Vertical advection of relative vorticity is never significantly different from zero (plot 2). At times the residuals (plot 5) are considerable, and

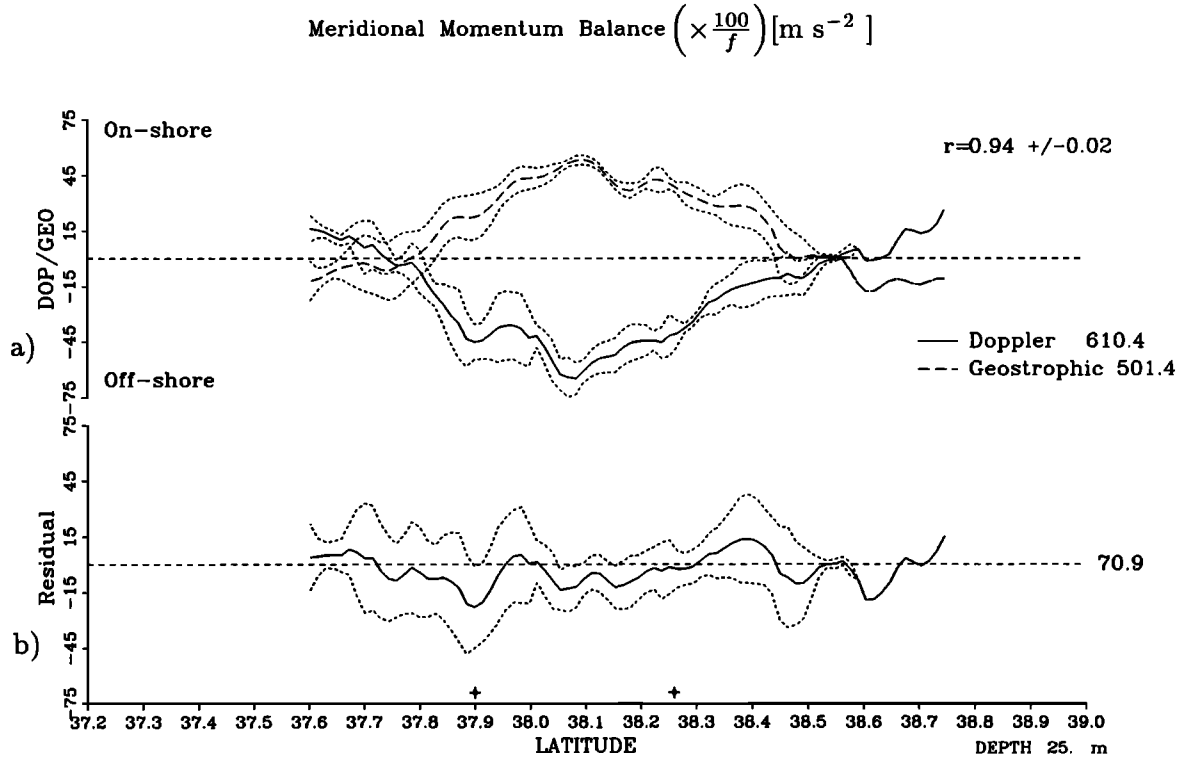

Fig. 11. (*a*) Mean zonal velocities and estimated meridional pressure gradient (geostrophic velocities) from three consecutive transects (between July 10 and 14) during Phase 1 indicating the possible ageostrophy implied by a reduction in the number of observations. The mean ADCP velocity U (solid line) and the negative "geostrophic" velocity $-U = (1/f\rho_0)\partial P/\partial y$ (long-dashed line) are each shown with 95% confidence intervals. (*b*) The geostrophic residual (difference of series in Figure 11*a*) with the summed 95% confidence interval. The correlation is $r = 0.94$ with a 95% confidence interval of 0.02. An estimated 15 independent observations imply a correlation $|r| > 0.51$, significantly different from zero at the 95% level. At the right of the labels and the residual are the series variances in $cm^2\ s^{-2}$.

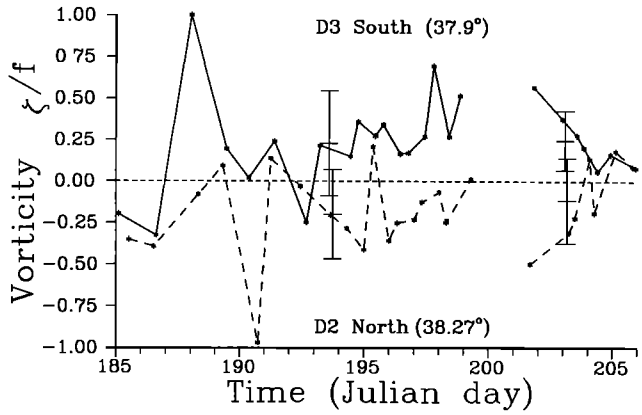

Fig. 12. Time series of the relative vorticity ζ calculated from the ship and moored ADCP velocity vectors and scaled by $1/f$. The northern location (D2, dashed line) shows consistent negative vorticity, the southern location (D3, solid line) shows consistent positive vorticity. The very large negative value during Julian day 190 at D2 is believed to be a result of poor ship navigation. Averages for each location and filament orientation are shown with confidence intervals of 1 standard deviation.

the horizontal advection terms $(U\partial\zeta/\partial x)$, $(V\partial\zeta/\partial y)$, not estimated, are expected to contribute significantly to the dynamics in reducing this residual. Without these contributions, we are unable to close the balance or estimate our "noise" residual. Even without the two advection terms, the variability in the observed contributions results in temporal mean and residuals insignificantly different from zero.

During the transition from phase 1 to phase 2 (on or about (±2 days) July 18, Julian Day 200) the relative vorticity south (D2) of the filament core (Figure 12) remained near $\zeta = 0.5f$. North (D3) of the core the vorticity decreased (from $\zeta \simeq 0$ to $\zeta = -0.4f$), but the rate of change $\partial\zeta/\partial t$ is no larger than that observed at other times (Figure 13*b*; July 5, Julian day 187). Despite the density of observations resulting from the repeated transects (estimates every 1–2 days), the variability in the vorticity appears to be undersampled (Figure 13*b*, plot 1). Within the core of the filament, maximum surface speeds were of the order of 1 m s^{-1}, or ~80 km d^{-1}, which suggests that mesoscale structures could easily have been advected by the observation sites between transects, aliasing the daily estimates. Drifter data provide a Lagrangian perspective of vorticity [*Paduan and Niiler*, 1990; M. Swenson et al., Drifter observations of the dynamical and thermodynamical structures in a cold filament off Point Arena, California, in July 1988, submitted to *Journal of Geophysical Research*, 1990, hereinafter referred to as Swenson et al., submitted) that at first seems more stable, but drifter groups are selected subjectively and tend to accumulate in regions of convergence, again aliasing the vorticity field.

5. Discussion

The analysis of the meridional component of momentum indicates two levels of geostrophy, corresponding to two components in the filament coordinates (across and approximately along filament). During phase 1 the hydrographic sections resolved the maximum pressure gradient. The average meridional momentum field was found to be highly geostrophic. Ageostrophic contributions to the momentum balance were determined to be below the noise level of the measurements, with only 6.5% of the variance in the meridional momentum equation unexplained. The meridional momentum analysis during phase 2, representing approximately the along-filament component, indicates a significant increase in the level of ageostrophy. The residual during phase 2 represents 15% of the total variance.

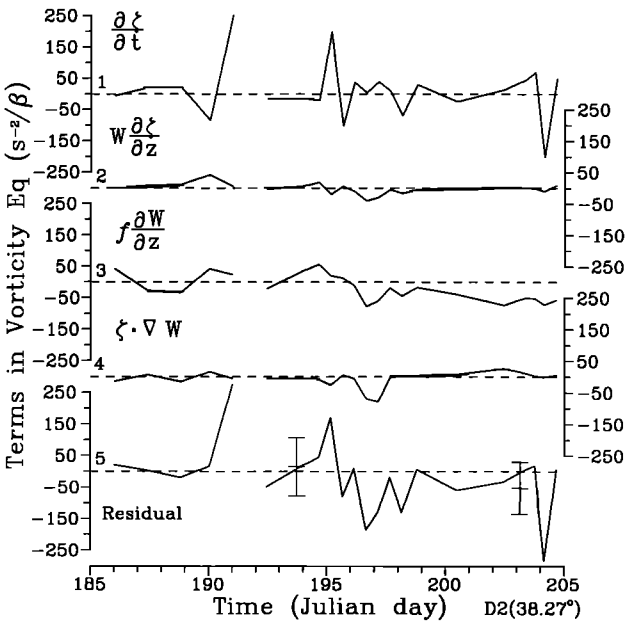

Fig. 13*a*

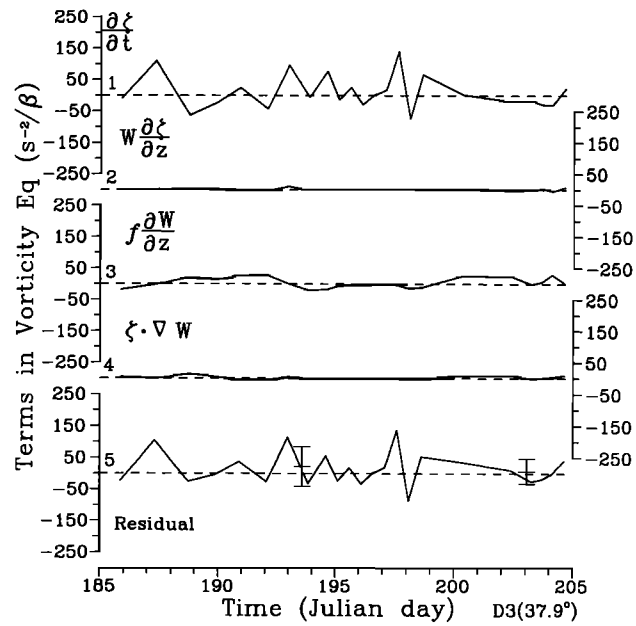

Fig. 13*b*

Fig. 13. Estimated terms in the vorticity equation scaled by $1/\beta$ for (*a*) the northern location (D2) and (*b*) the southern location (D3). In order, they are (1) the observed rate of change $\partial\zeta/\partial t$, (2) vertical advection $W\partial\zeta/\partial z$, (3) the stretching of planetary vorticity $f\partial W/\partial z$, (4) the tilting and stretching of relative vorticity $(\xi\partial W/\partial x + \eta\partial W/\partial y + \zeta\partial W/\partial z)$, and (5) the sum of all estimated terms representing the residual (less the mean horizontal advection of relative vorticity). Also shown are two temporal averages of the residual term for phases 1 and 2 with uncertainties of 1 standard deviation.

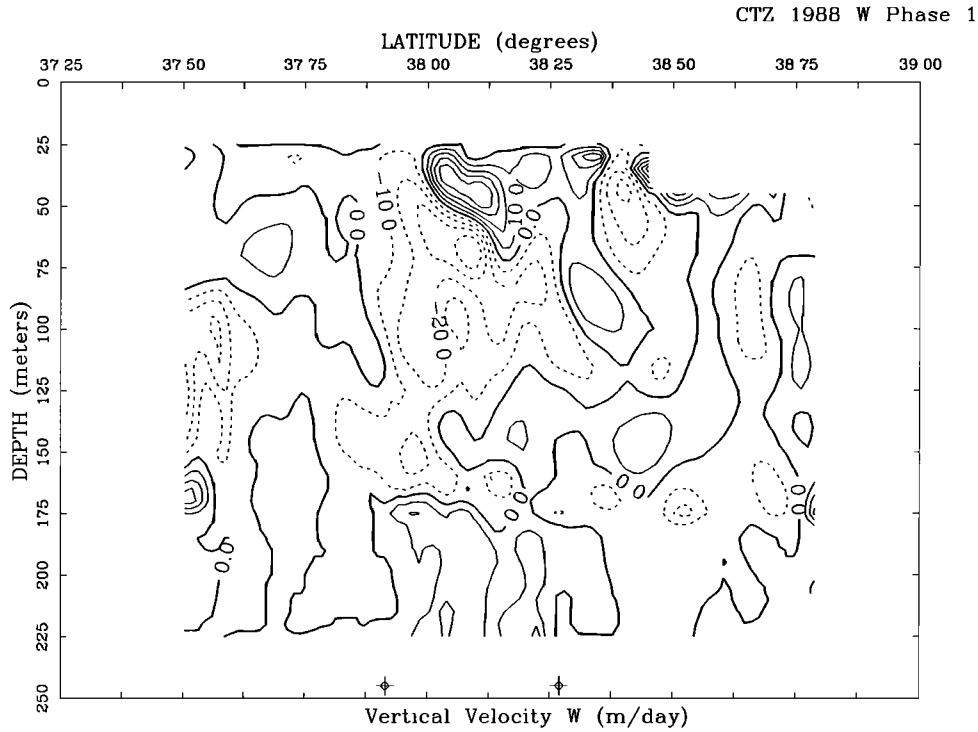

Fig. 14. Mean vertical velocities (in meters per day) during phase 1 calculated using (B4). Solid contours indicate positive (upward) velocities, dashed contours negative (downward) velocities. Maximum vertical velocities are ~40 m d^{-1}. The surface region north of 38.4° latitude has been blanked because of the deep surface mixed layer that exists there, resulting in very low buoyancy frequencies (N^2) and inaccurate W estimates. Uncertainties derived from the variations in individual contributions to W are of the order of ± 10 m d^{-1}.

The only significant feature revealed by the vorticity analysis is the persistent asymmetry of the filament. Ship and moored ADCP observations were used to estimate the total relative vorticity on either side of the filament core. Larger (magnitude) positive relative vorticity was consistently observed on the south (cool) side of the front.

An interesting result of the momentum analysis is the estimation of the mean vertical velocity section across the filament (Appendix B). Because of their small magnitude, vertical velocities are difficult to measure and estimate, yet may play important roles in many aspects of the physics and biology associated with fronts. The subduction of nutrient rich coastal water (recently upwelled), along the filament [*Washburn et al.*, this issue; B. Jones et al., Chemical and biological structure of a cool filament observed off northern California in July 1986, submitted to *Journal and Geophysical Research*, 1990) and the divergence and convergence implied by drifter groups (Swenson et al., submitted) are examples of studies directly dependent on the distribution of vertical velocities within the filament.

The estimated vertical motions were mostly driven by adjustments in the relative vorticity (Appendix B) and simply represent the vertical component of near-geostrophic flow along sloping isopycnal surfaces. Within the central region of the filament, where the data density (temporal) is highest and the estimates are significantly different from zero, three dominant regions of W exist (Figure 14). Coinciding with a horizontal velocity maximum (Figure 5*d*, 38.1°) is a region of upwelling (10–40 m d^{-1}), bounded on either side (and below) by regions of downwelling. Broad regions of relatively high vertical velocities (40 m d^{-1}) are predicted in the filament models [e.g., *Walstad et al.*, this issue; *Haidvogel et al.*, this issue], but poor spatial resolution in the models limits a direct comparison with our estimates.

Individual water packets do not remain in these high vertical velocity regions for long periods and only "slide" up (or down) for several hours, resulting in vertical excursions of perhaps 10–20 m (D. Haidvogel, personal communication, 1990). These regions of vertical motion are typically tens of meters (20–100 m) thick and tens of kilometers wide. They appear consistently in the repeated sections (although they vary in magnitude and shape), indicating persistent underlying recirculations, due mostly to adjustments in vorticity. Individual sections of W, T, and S often have high correlations between interleaving temperature-salinity intrusions and implied regions of upwelling and downwelling, an independent indication that (B4) predicts real vertical velocity structure. A separate study of the intrusive activity will follow in a future paper.

One feature revealed by the multiple transects across the filament is the position of the surface temperature minimum relative to the salinity minimum and maximum. During phase 1 the maximum mean zonal velocity at a depth of 25 m occurred at approximately 38.1° latitude (Figure 15*a*), with a magnitude of ≈ -65 cm s^{-1}. This location corresponds exactly with the maximum meridional density gradient, in accordance with geostrophy. On closer inspection, the position and relative shape of the temperature and salinity extrema reveal important characteristics that can be explained through cross-frontal exchange.

The salinity maximum is slightly offset to the south of the velocity core, a region between 37.75° and 38.0° latitude

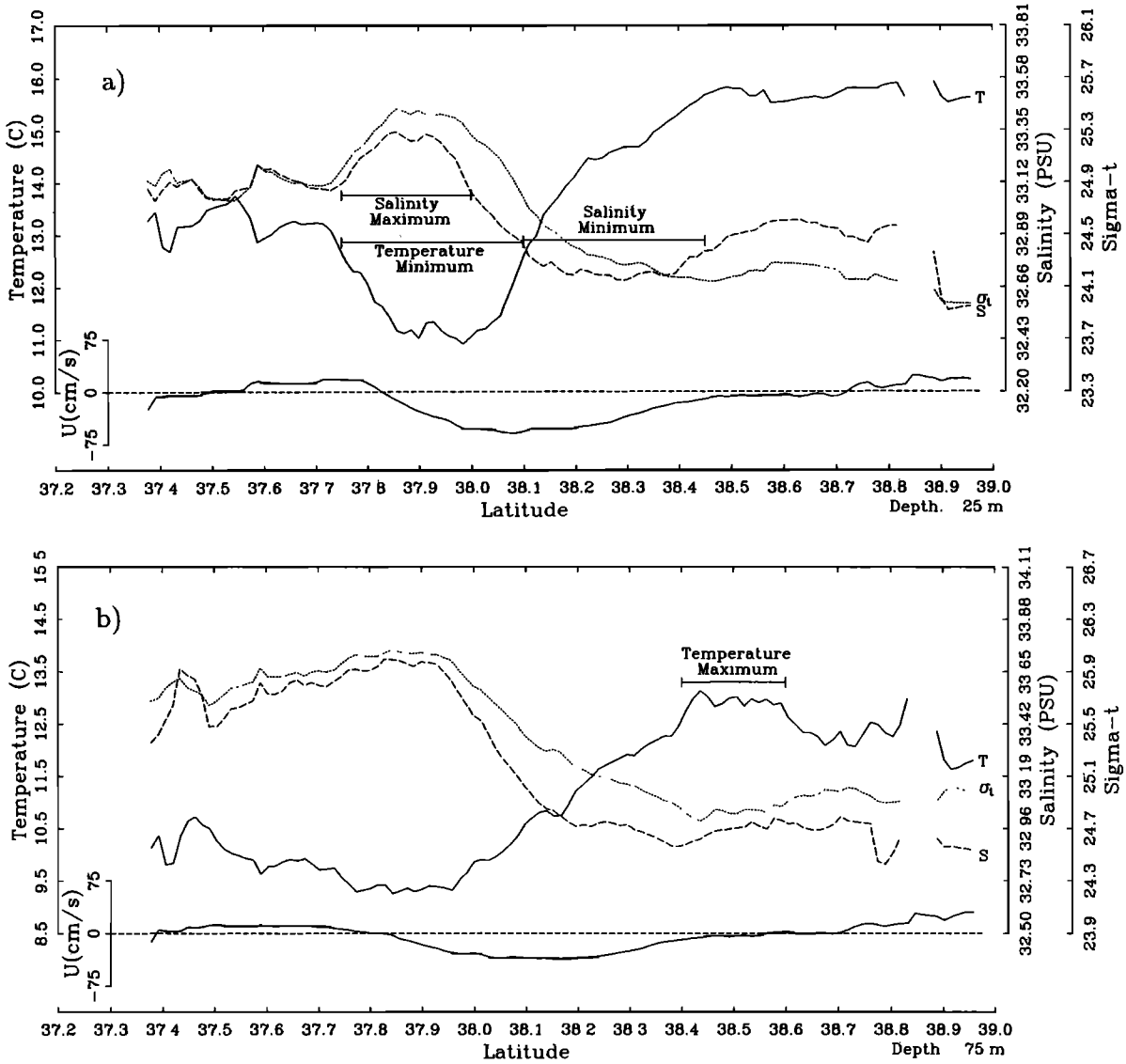

Fig. 15. Spatial series of the average temperature (T), salinity (S), σ_t, and the zonal velocity (U) at (a) 25 m and (b) 75 m depths for phase 1 (July 2–16, 1988) along the D line. The temperature and salinity scales have been chosen to represent equal contributions to variations in the density (or σ_t). Of special interest are the relative positions and shapes of the salinity maximum and temperature minimum to the south and the salinity minimum just north of the maximum zonal velocity.

(Figure 15*a*). Similarly, the temperature minimum is south of the maximum current, but significantly broader (37.75° to 38.1° latitude) than the salinity maximum. To the north of the current maximum there is a local salinity minimum, between 38.1° and 38.45° latitude. Fresher surface water is therefore being transported on the north (negative relative vorticity) side of the filament, while the colder, more saline surface water is confined to the south (positive vorticity) side of the filament. This asymmetric structure appears to be a persistent feature of the upwelled fronts in this region and is discussed further by *Strub et al* [this issue].

The mean structure at 75 m depth (Figure 15*b*) is significantly different than the surface structure, and the three local extrema are less identifiable; yet the overall range of temperature, salinity, and σ_t across the filament remain similar (Figure 15*a*). In the deeper section (Figure 15*b*) the only anomalous feature distinct from the main front is a small temperature maximum within the northern extreme of the offshore flow (38.4° to 38.6° latitude).

Coastal upwelling is believed to be the main source of potential energy for these filaments, bringing cool, saline water to the surface over the continental shelf. Once separated from the shelf, coastal (Ekman) upwelling ceases. During coastal upwelling, temperature-salinity extrema are highly correlated [*Huyer and Kosro*, 1987], as they are in the mean structure at 125 m (Figure 3*b*). The near-surface distribution of temperature and salinity (Figure 15*a*) has apparently undergone a transformation since the water was upwelled near the coast. The salinity maximum, south of the current maximum, is considerably narrower than the associated temperature minimum (Figure 15*a*), indicating the mixing of different water masses. Local upwelling/downwelling (divergence/convergence) is a candidate for bringing different water masses together (stirring); near-

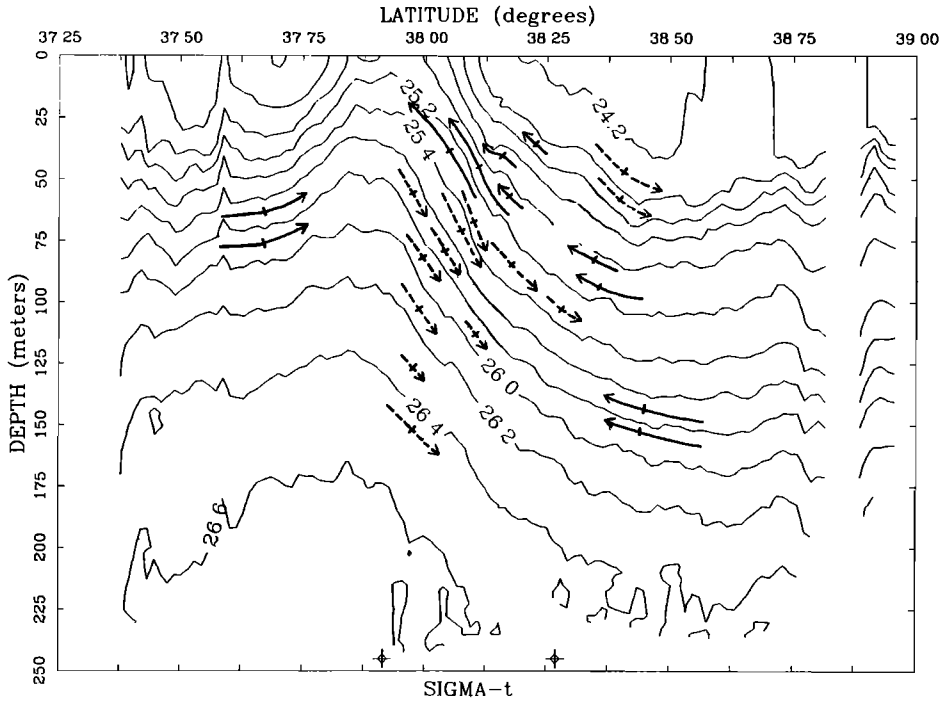

Fig. 16. Contours of the mean density (as in Figure 5c) during phase 1 (July 2–16, 1988) along the D line. Superimposed are vectors representing the possible "isopycnal" flow suggested by the meridional ADCP velocity sections and the estimated vertical velocities (Figure 14). The vectors have been drawn parallel to the isopycnal surfaces and scaled so that the vertical component represents the daily vertical displacement centered at the mark on each vector.

surface, wind-driven turbulence is likely the only available mechanism for the mixing [*Moum et al.*, 1988; *Dewey and Moum*, 1990]. The estimated mean vertical velocity W (Figure 14) and the implied cross-frontal circulation, can explain some of the structure in the observed surface distributions.

The mean σ_t structure for phase 1 is shown in Figure 16. Superimposed are conceptual velocity vectors showing flow along isopycnal surfaces as indicated by the mean estimates of V and W (Figures 5e and 14 respectively). The arrows (Figure 16) were not measured directly, but are estimates scaled so that the vertical component represents the daily vertical displacement.

Zonal isopycnal slopes (not resolved by the meridional transects) may contribute significantly to W, and the regions of estimated upwelling (downwelling) have been interpreted simply as flow along the resolved isopycnal surfaces (Figure 16). Nonetheless, for a descriptive explanation we require only a conceptual picture of the possible flow. In the depth range 25–100 m, three regions of upwelling are evident (Figure 16). Near the central region of the front (50–125 m, 37.9°–38.3° latitude) is a downwelling region, narrower at 50 m, expanding to a wider region at depth (100 m, Figures 14 and 16). A second, smaller downwelling region is evident north of the strongest upwelling. The central upwelling region (Figure 16) implies cross-frontal flow from the north side of the velocity maximum (38.1° latitude) along isopycnal surfaces towards the uplifted dense core of the filament to the south (37.85°–38.0°)

A possible mechanism responsible for causing the observed asymmetric temperature minimum and salinity maximum on the south side of the filament core (Figure 15a) is the mixing of the cooler (subsurface) part of the fresh pool from the north side, with the shallower water found on the upwelled side (south) of the filament. Observations (Figure 15a, also *Hayward and Mantyla* [1990] and *Strub et al.*, [this issue]) indicate the presence of a pool of fresher, cool water on the seaward side of upwelled fronts along the California coast. This pool is typically confined to the upper 60 m and is 20–30 km wide. It is believed this fresher water may originate at the Columbia river mouth (some 1000 km to the north), where it is ejected onto the continental shelf and then flows southward, remaining on the outer edge of the upwelling (divergent) region and the subsequent front that is formed by the upwelling.

If the internal upwelling region near the zonal velocity maximum in Figure 16 were to bring fresher and cooler water from the north, up along isopycnals to the surface on the south side of the velocity maximum, wind-induced turbulent mixing could then produce the observed temperature-salinity distributions. Observed turbulent dissipation rates have been low within these upwelled filaments, below the wind driven surface layer [*Moum et al.*, 1988; *Dewey and Moum*, 1990]. The only persistent turbulent region is the near surface mixing layer driven by wind stresses. The fresher water found at the surface, north of the velocity maximum (Figure 15a) may be maintained by the convergence implied by the region of local down-welling (Figure 14) between 38.3° and 38.4° latitude. The local temperature maximum at depth (75 m, Figure 15b) may originate nearer the surface on the south side of the velocity maximum, where it is then advected downward along isopycnals in the downwelling region indicated in Figures 14 and 16.

The asymmetry in the temperature-salinity distributions

north and south of the current maximum indicate that temperature measurements alone are insufficient in determining the density structure. Salinity variations play a crucial role in determining the local density structure and therefore the dynamic height fields. Thermal satellite images, revealing only the surface temperature structure, may be less representative of the density structure away from the coastal upwelling region, where internal circulations within the filament-current system can redistribute and mix water types, modifying the relative roles of temperature and salinity in governing the local density.

6. Conclusions

During July 2–23, 1988, a significant upwelled filament was observed in two substantially different orientations. The observations during each filament orientation have been used to estimate average terms in the meridional momentum balance. During phase 1 the current component perpendicular to the transect line was found to be in geostrophic balance. During phase 2 the meridional data closely represent a coordinate system along the axis of the filament, and the meridional momentum balance was found to be significantly more ageostrophic. Observed acceleration and cyclostrophic contributions to the momentum balance (i.e., $\partial V/\partial t$ and $V\partial VG/\partial y$) were significantly above the estimated noise levels at a number of locations during phase 2.

Although it appears that a considerable effort has been exerted to show the near-surface (<150 m) currents associated with these fronts are highly geostrophic, the results are by no means serendipitous. The strong currents, narrow structure, relatively large Rossby number ($U/Lf \simeq 0.3$), and temporal variability of these upwelled fronts suggests that quasi-geostrophic dynamics may play a significant role. Despite these structural characteristics, the present analysis indicates a highly geostrophic flow. The measurements analyzed here represent a unique set of observations, ideal for examining the dynamics of fronts. To our knowledge, the present analysis also represents a unique attempt to complete a momentum balance.

Mean vertical velocities are estimated from the multiple transects using ship ADCP and RSVP hydrographic and turbulence data (Appendix B). The calculation is made possible by the temporal resolution of observations in a near-geostrophic flow field. Previous estimates of W utilized only moored current measurements. The estimated vertical velocities from the ship observations are in agreement with model predictions.

Relative vorticity is estimated from moored and ship ADCP measurements. During the microstructure survey, the northern mooring location is found to remain in the negative relative vorticity shear of the filament, while the southern mooring remains in the positive relative vorticity. The mean magnitude of the positive vorticity ($0.25f$) is larger than the mean magnitude of the negative vorticity ($-0.16f$), a possible consequence of instabilities that work preferentially in regions of negative vorticity.

Finally, the repeated transects of high-resolution hydrography reveal temperature and salinity distributions that suggest considerable recirculation within and across the filament. Local adjustments in the relative vorticity may cause submesoscale divergences and convergences that result in upwelling and downwelling along isopycnal surfaces. The resulting redistribution of water masses may form the narrow, near surface (<50 m) salinity maximum embedded in a broader temperature minimum, both confined to the region south of the current maximum. Confined to a region north of the current maximum was a "pool" of less saline water. The influence of the observed salinity structure on the density field (and therefore the pressure and dynamic height fields) cannot be revealed by thermal remote sensing (advanced very high resolution radiometer).

Appendix A: Calculations for Momentum Analysis

Our coordinate system is right-hand Cartesian, aligned with the hydrographic survey grid. It is a simple rotation of standard linear Earth coordinates (x = east, y = north) by 30° counterclockwise. In this system, x = east-northeast, perpendicular to the D line, and y = north-northwest, along the D line. The transformation from measured "Earth" coordinate velocities (U_e, V_e) is then

$$U = U_e \cos(30°) + V_e \sin(30°), \qquad \text{(A1}a\text{)}$$

$$V = V_e \cos(30°) - U_e \sin(30°). \qquad \text{(A1}b\text{)}$$

Under this transformation, the momentum equations (1) are unchanged, and "meridional" will now refer to the new y direction. As a result of this rotation, D line latitude is slightly stretched from normal latitude such that 1.0° "latitude" ≃ 128 km. During phase 1 the orientation of the filament is such that water "north" of the velocity maximum represents warmer, offshore, nonupwelled water, and water "south" of the velocity maximum represents cooler, coastal upwelled water.

To minimize and quantify errors, the repeated transects during each phase were used to provide multiple estimates of each momentum term from which mean values were calculated. Simple statistical analysis was used to estimate the variabilities and uncertainties. The estimated mean of each term for each filament phase is bounded by an uncertainty derived from the variability of the individual estimates. A full meridional momentum balance [i.e., (1b)] can be estimated from a minimum of two transects (in order to estimate $\partial V/\partial t$); however, no statistical confidence can be assigned to the terms in a two-transect balance. Including more transects in the analysis increases the confidence, at the expense of resolving variability on short time scales.

Since the number of independent observations is limited, error statistics are calculated using a bootstrap technique [*Efron and Gong*, 1983, *Efron*, 1987]. The procedure simply calculates the mean of n estimates of the appropriate statistic (i.e., mean, variance, or correlation coefficient) calculated from i random selections from the original ensemble of i estimates. A bootstrap iteration of 500 was found to give stable results. In other words, to estimate the confidence interval for the mean of a quantity at a fixed location from i transects, 500 ($=n$ estimates of the mean were calculated from 500 ensembles of i random selections from the original i estimates. The final mean is then the mean of the 500 estimated means (insignificantly different from the sample mean), and confidence limits (95%) can be selected directly from the bootstrap distribution of means.

When estimating statistics for terms in the momentum balance from multiple transects it is assumed that the dynamics are reasonably stationary during that period and that the variability of the estimates reflects natural uncertainty rather than a trend about the mean. To test the validity of

this presumption for phase 1 (July 2–16), three momentum analyses were performed on successive groups of four consecutive transects. No trend was found, and the inclusion of all nine transects in a single momentum analysis was deemed justifiable.

One final note about the analysis to follow. Some of the terms in the momentum equation (1*b*) were calculated using both RSVP (hydrographic) and ADCP (velocity) data ($W\partial V/\partial z$ and $(1/\rho_0)\nabla \cdot \tau_{yi}$), one term from RSVP data only ($-(1/\rho_0)\partial P/\partial y$), and some terms from ADCP data only ($\partial V/\partial t$, $U\partial V/\partial x$, $V\partial V/\partial y$, fU). Therefore although we have nearly twice the density (in time) of ADCP observations to RSVP observations (northward and southward transects as opposed to northward only), we use only coincident data (collected simultaneously during the northward-heading transects). This assures that the estimated contributions to the momentum balance represent observations of the same "field."

There were 10 northward heading RSVP/ADCP transects attempted during Phase 1 (July 2–16). Of these, one was aborted prematurely (transect 4, after only 30 km) and during the eighth transect, instrument problems kept the RSVP out of the water. Therefore in the momentum analysis, eight complete transects and one short transect make up the data during phase 1; three complete transects make up phase 2 (July 20–23).

The first ageostrophic term in (1*b*) is the net acceleration, $\partial V/\partial t$. By repeating transects every ~1–2 days we estimate the acceleration by first-differencing ADCP estimates of V at each position (y) between consecutive transects (δt). During the northward-heading transects, when both RSVP and ADCP data were collected, the ship speed ranged between 2.5 and 5 knots (~1.2–2.5 m s^{-1}). At these speeds, the averaged (gridded) ADCP profiles have separations of 1.8 km horizontally and are equivalent to 15-min averages. Although the estimated uncertainty in 15-min ADCP velocity averages is about 8 cm s^{-1}, first-differencing these velocity estimates over periods of 1–2 days results in relatively larger uncertainties in the acceleration (small differences between large quantities). The errors are reduced by averaging several estimates, each obtained from a first difference between consecutive transects. Of the nine transects during Phase 1, eight were complete, resulting in seven estimates of $\partial V/\partial t$ at each location (both in y and z). Had the M_2 tide not been removed from the shipboard ADCP data, aliasing would have contributed fictitious accelerations (tidal) as large as $(\partial V/\partial t)/f \simeq 10$ cm s^{-1}.

The second ageostrophic term in (1*b*) represents zonal advection of meridional momentum ($U\partial V/\partial x$). The meridional transects do not provide direct information on the zonal gradients. Only at the two ADCP mooring locations do we have zonal gradient information on U and V. Therefore for each transect and each mooring location, an estimate of $U\partial V/\partial x$ is made from the mean $\bar{U}$ between mooring and the ship track and the first-difference gradient $\partial V/\partial x$ between the two locations. The moored ADCP velocities were averaged over 1.5-hour periods centered when the ship passed the y location of the mooring. The spatial (ship) ADCP data was averaged over the same interval, representing approximately ~12 km of ship track. The average minimum distance between the ship track and the moorings was ~4.6 km.

The ageostrophic component of the meridional momentum balance $V\partial V/\partial y$ is estimated directly from the shipboard ADCP measurements. Measured V along the ship track (y) is easily differenced to estimate $\partial V/\partial y$. Estimates of the mean gradient across both three and five consecutive 15-min-average profiles were compared and the gradient across three was used, as it was insignificantly different from the broader gradient estimate.

The flux divergence term represents turbulentlike (eddy) processes that act to redistribute momentum. Here it is parameterized through the gradient of the Reynolds stress τ. This is an important term when wind forcing directly influences the near-surface flow, as the surface stress (momentum flux) is translated to the flow through turbulent diffusion. This term also represents the momentum flux from submesoscale eddies. Although such contributions may be significant, we have no means of accurately estimating them for the limited period of our measurements.

A useful parameterization of Reynolds stresses is to assume that the momentum flux at turbulent scales acts like molecular diffusion, and the stress components can be approximated by eddy viscosities working on local velocity gradients. As a consequence of this parameterization, the horizontal eddy viscosities are much larger than the vertical equivalent because of the much weaker horizontal shears. Although oceanic models often require adjustable horizontal viscosities to match observed flux rates, applicable parameterizations for measured oceanic shears (horizontal) have yet to be verified and are typically ignored [*Gregg*, 1987].

Parameterizing a vertical eddy viscosity is more common, where the vertical turbulent momentum flux ($\tau_{yz} = -\overline{\rho v' w'}$) is approximated by $\rho K_m \langle \partial V/\partial z \rangle$, where K_m is the vertical eddy viscosity and the angle brackets denote an appropriate averaging process that eliminates short time scale fluctuations in the mean shear (internal waves, noise) but not general trends. An estimate of K_m is obtained from the steady state turbulent kinetic energy equation, where turbulence production is assumed to be balanced by viscous dissipation [*Osborn*, 1980; *Crawford*, 1982; *Dillon et al.*, 1989],

$$K_m \left\langle \frac{\partial \mathbf{U}}{\partial z} \right\rangle^2 \simeq \langle \varepsilon \rangle, \tag{A2}$$

where $\langle \partial \mathbf{U}/\partial z \rangle^2 = \langle \partial U/\partial z \rangle^2 + \langle \partial V/\partial z \rangle^2$ is the total vertical shear variance. Dissipation rate estimates from the RSVP profiles and shear estimates from the ADCP measurements are combined to give estimates of the vertical eddy viscosity.

The full flux divergence in (1*b*) is approximated by the vertical flux divergence of small-scale meridional momentum given by

$$\frac{1}{\rho_0} \nabla \cdot \tau_{yi} \simeq \frac{1}{\rho_0} \frac{\partial \tau_{yz}}{\partial z} = \frac{\partial}{\partial z} \left(\frac{\langle \varepsilon \rangle \langle \partial V/\partial z \rangle}{\langle \partial U/\partial z \rangle^2 + \langle \partial V/\partial z \rangle^2} \right). \tag{A3}$$

This formulation has been used in the analysis of equatorial dynamics, where the flow is not constrained by Coriolis accelerations [*Crawford*, 1982; *Gregg et al.*, 1985; *Dillon et al.*, 1989]. Here, the individual sections of ε and ADCP shear are combined and the flux divergence estimated.

The final ageostrophic term in the meridional momentum equation (1*b*) to be estimated is the vertical advection of meridional momentum, $\langle W \rangle \langle \partial V/\partial z \rangle$. The vertical shear in V is obtained by differencing the ADCP measurements, as was described above The vertical velocity W is not measured, but a mean value can be estimated using both the RSVP hydrographic data [$\rho(z)$] and the ADCP velocity (U, V)

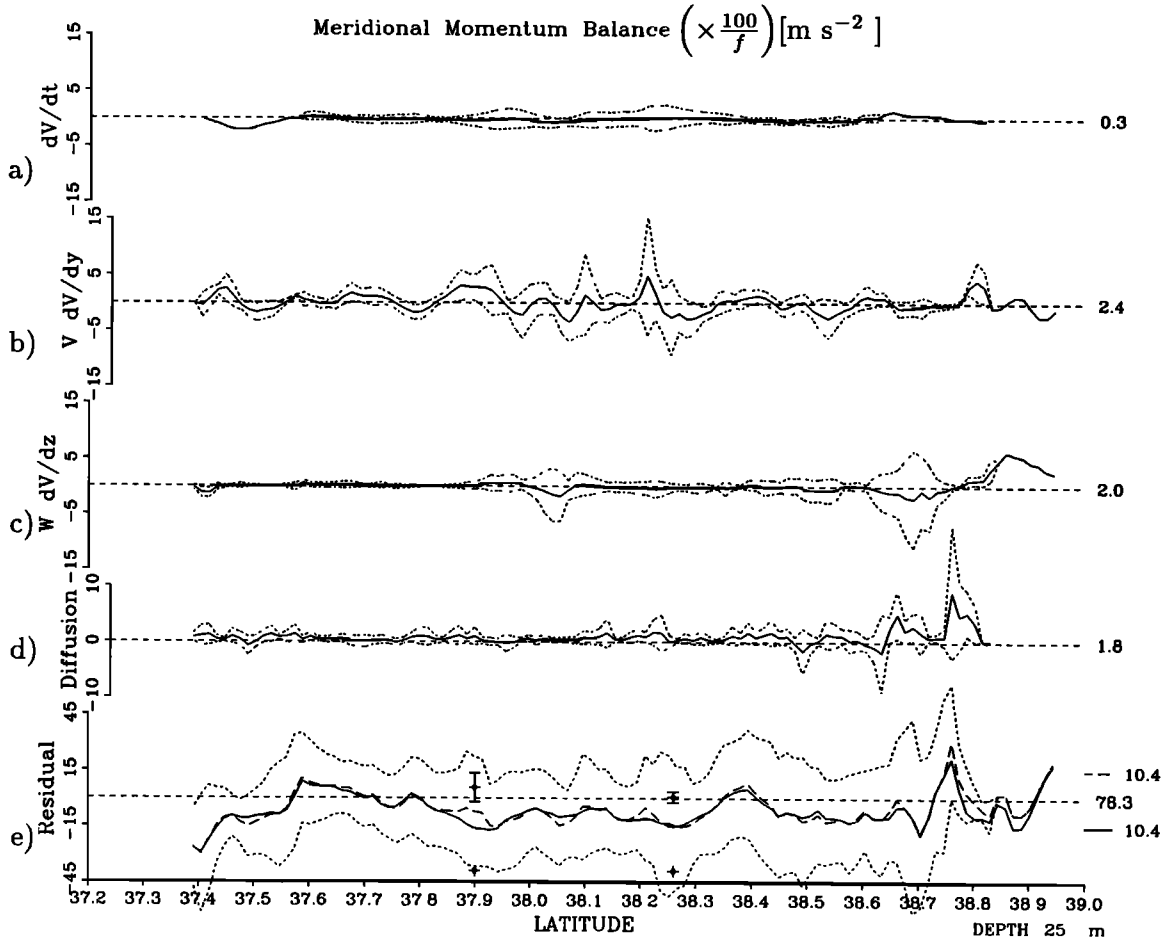

Fig. 17. Temporally averaged ageostrophic contributions (in centimeters per second) to the meridional momentum balance at 25 m during phase 1, with 95% bootstrap confidence limits. To the right are the series variances (in cm^2 s^{-2}). (*a*) The average acceleration $\partial V/\partial t$, not significantly different from zero. (*b*) Meridional advection $V\partial V/\partial y$, showing narrow regions of significance. (*c*) Vertical advection $W\partial V/\partial z$, with two regions of high variability, but insignificantly different from zero. (*d*) Vertical mixing, almost always positive (deceleration), yet never significantly different from zero. (*e*) "Geostrophic" residual (solid) from Figure 7*b*, and total residual (dashed) after including the ageostrophic contributions. Shown above the two mooring locations are the estimates of zonal advection $U\partial V/\partial x$, with 95% confidence intervals. At both locations the zonal advection acts to reduce the final residual. Also shown at the right are the rms values for the geostrophic and final residuals.

measurements. Since this calculation has not been verified by in situ measurements of W and may not be universally accepted (or known), Appendix B is dedicated to a thorough description of the formulation and calculation.

Unique in the present analysis of the meridional momentum terms, the vertical advection term is calculated once for each filament orientation. This is due to the temporal mean required in estimating reliable vertical velocities. The temporal means, $\langle W\rangle$ and $\langle\partial V/\partial z\rangle$, are then multiplied and confidence limits are determined from the uncertainty of individual constituents leading to the final product. It is acknowledged that $\langle W\rangle\langle\partial V/\partial z\rangle$ is not equivalent to $\langle W(\partial V/\partial z)\rangle$. Because of the temporal averaging required to estimate reliable vertical velocities (Appendix B), the product of the mean values is deemed a reasonable approximation to the mean of the product in light of the stationary character of the filament during the two phases.

Before looking at the estimated ageostrophic contributions, we should establish the expected error level for each term due simply to measurement uncertainty. Assuming that measurement errors are random and normally distributed, the error variance for any particular measurement will simply be $\sigma_e^2 \simeq (e/2)^2$, where e is an estimate of measurement uncertainty. For example, given that the ship ADCP velocities have a uncertainty of ± 8 cm s^{-1}, the error variance for U is approximately 16 cm^2 s^{-2}. Therefore, an estimated variance less than $\sim$16 cm^2 s^{-2} for a scaled fU term is at or below the expected measurement noise level. The multiple transects and observations are treated as an ensemble and an uncertainty in a mean estimate from N transects will be reduced by $(N-1)^{-1/2}$. For certain product terms (i.e., $U\partial V/\partial x$), the errors can be assumed to be independent and the error variance is then the sum of the individual variances divided by $2^{1/2}$. Consequently, the estimated variance noise levels for the remaining meridional momentum terms are (after scaling by $100/f$) 12 cm^2 s^{-2} for $-(1/\rho_0)\partial P/\partial y$, 18 cm^2 s^{-2} for $\partial V/\partial t$, 24 cm^2 s^{-2} for $U\partial V/\partial x$, 30 for $V\partial V/\partial y$ (this variance, and others with similar products, is larger because V and ∂V are dependent and not random), 26 cm^2 s^{-2} for $W\partial V/\partial z$, and 24 cm^2 s^{-2} for $(1/\rho_0)\partial\tau_{yz}/\partial z$. Surprisingly, the ageostrophic terms do not have significantly larger measurement error variance than the geostrophic terms; however, no

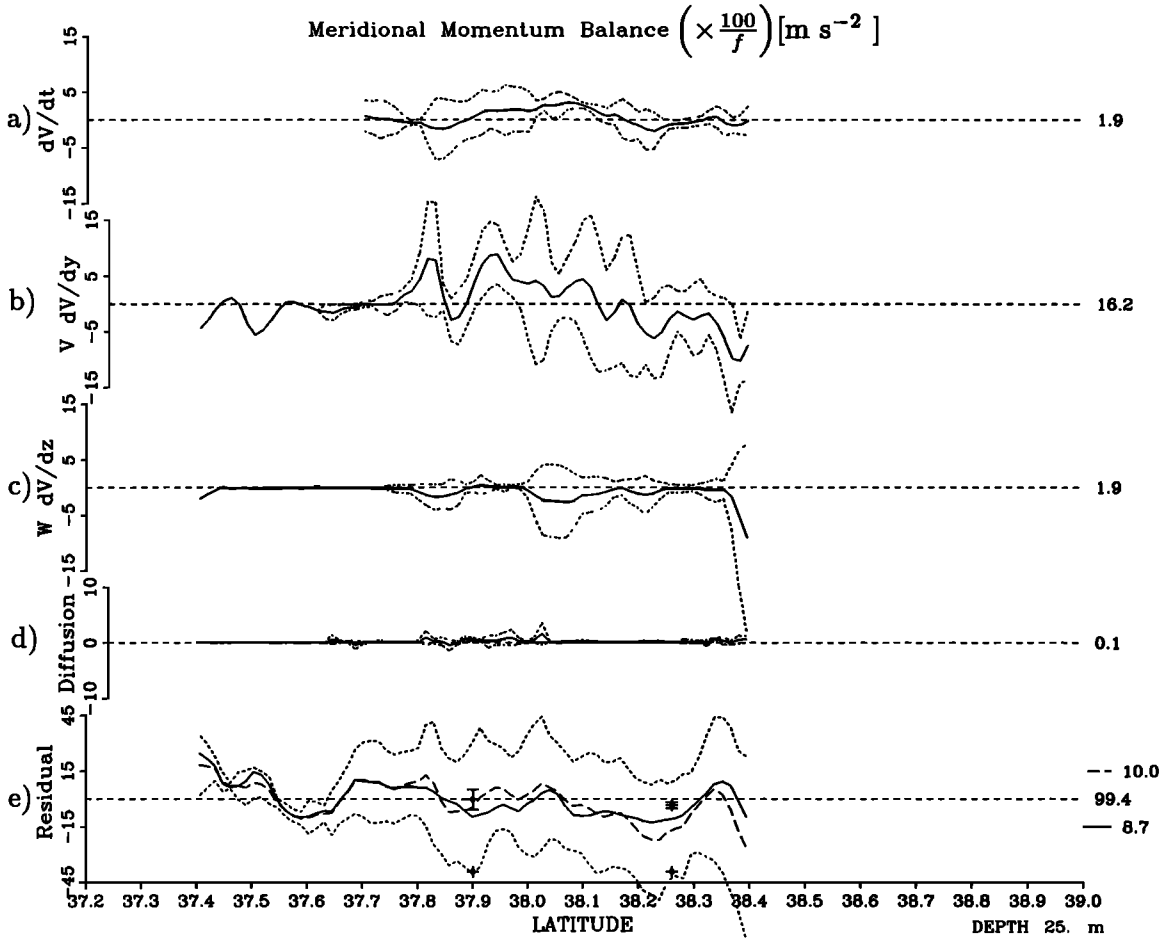

Fig. 18. Temporally averaged ageostrophic contributions (in centimeters per second) to the meridional momentum balance at 25 m during phase 2, with 95% bootstrap confidence limits. To the right are the series variances (in cm^2 s^{-2}). (*a*) The average acceleration $\partial V/\partial t$, now with a single region significantly different from zero. (*b*) Meridional advection $V\partial V/\partial y$, showing narrow regions of significance and a greatly increased variability. (*c*) Vertical advection $W\partial V/\partial z$, nowhere significantly different from zero. (*d*) Vertical mixing, clearly a very small ageostrophic component, insignificantly different from zero. (*e*) "Geostrophic" residual (solid line) from Figure 9*b*, and total residual (dashed) after including the ageostrophic contributions. Shown above the two mooring locations are the estimates of zonal advection $U\partial V/\partial x$, with 95% confidence intervals. During phase 2 the zonal advection contributes very little to the meridional momentum balance. Also shown at the right are the rms values for the geostrophic and final residuals, showing a significant increase in the variability, a result of the fewer observations during phase 2 as well as the influence of more variable ageostrophic contributions.

additional error has been added for the assumptions used in arriving at the terms. Bootstrapping multiple transects of each term also provides confidence limits representing the variability in the observations.

Mean values for the five ageostrophic terms for phase 1 (July 2–16) are shown in Figure 17. The stationarity of the filament over this two week period is reflected by the low estimates in the mean acceleration $\partial V/\partial t$ (Figure 17*a*). The highest variability (widest confidence interval) occurs near the center of the jet. The meridional advection term (Figure 17*b*) $V\partial V/\partial y$ is rarely significantly different from zero, with maximum magnitudes within the core of the jet. (Note that at the ends of certain momentum contributions (e.g., $V\partial V/\partial y$), the bootstrap confidence intervals collapse, indicating regions sampled only once.)

Both vertical advection and turbulent diffusion (Figures 17*c* and 17*d*, respectively) are negligible over most of the region, with maximum magnitudes to the north. This is a result of the deep mixed layer in the northern extent of the sections (Figure 5*c*). Large temporal changes in density ($\partial\rho/\partial t$) and weak stratification (low N^2) result in larger estimates of W and ε. Below 50 m, within the pycnocline, these terms are negligible. At both mooring locations the mean contributions from $U\partial V/\partial x$ are positive but are not significantly different from zero at a 95% level.

Root-mean-square values for the geostrophic and total residuals respectively are shown to the right in Figure 17*e*. The variance and rms for the geostrophic residual are 66.3 (cm^2 s^{-2}) and 10.4 (cm s^{-1}), respectively, and the variance and rms for the total residual are 78.3 (cm^2 s^{-2}) and 10.4 (cm s^{-1}), respectively. The additional four complete and two mooring location ageostrophic terms have not reduced the variance or rms of the momentum balance residual. The fact that the rms values are larger than the square root of the variances indicates a nonzero mean. If the individual ageostrophic terms represent random noise, the total variance would simply be the sum of the individual variances (66.3 + 9.8 = 76.1 cm^2 s^{-2}). The total residual variance (78.3 cm^2

s^{-2}) is insignificantly different from the sum of the individual variances that are below the estimated noise levels, indicating that the ageostrophic contributions to the meridional momentum equation are indistinguishable from random noise and below the noise level of calculation (measurement). Some variance (perhaps a considerable amount) is omitted by estimating the zonal advection at only two locations, although the indication (Figure 17*e*) is that this contribution may still be insufficient to balance the "noise" summed in the final residual.

Mean values for the five ageostrophic terms for phase 2 (July 20–23) are shown in Figure 18. During phase 2, the meridional advection term has considerably more variance (Figure 18*b*), a result of the filament turning more north-south and increased V (Figure 2*b*). The total residual (Figure 18*e*) has a variance of 99.4 $cm^2\ s^{-2}$, again nearly equal to the sum of the individual ageostrophic variances. The increase in residual variance is greater than the sum of the individual noise variances, indicating that certain ageostrophic terms are contributing significant variance but not consistently reducing the rms of the final residual. Both the mean acceleration (Figure 18*a*) and the meridional advection (Figure 18*b*) have regions significantly different from zero at the 95% level, and yet they are not always of the right sign to reduce the residual. In particular, the magnitude of the total residual is smaller than the geostrophic residual in the southern section (37.9°–38.15°) but larger to the north (38.2°–38.4°). The variance of the final residual now represents 18% of the observed variance. Again, the total variance is still missing some contributions from the zonal advection, sampled only at two locations.

Appendix B: Estimating the Mean Vertical Velocity W

The following technique for estimating the mean vertical velocity W was first reported by *Bryden* [1976] and was subsequently used in vorticity analyses by *Bryden* [1980], *Hall* [1986], and *Freeland and McIntosh* [1989]. The formulation is extended here by including contributions to the mean vertical velocity due to vertical mixing.

Vertical velocities can be estimated by considering the conservation of mass in an Eulerian reference frame. The conservation of mass can be written,

$$\frac{\partial \rho}{\partial t} + U\frac{\partial \rho}{\partial x} + V\frac{\partial \rho}{\partial y} + W\frac{\partial \rho}{\partial z} = \frac{\partial}{\partial z}\left(K_\rho \frac{\partial \rho}{\partial z}\right), \qquad \text{(B1)}$$

where ρ is the density and turbulent diffusion has been approximated by the divergence of the local vertical turbulent diffusion coefficient working on the local vertical density gradient.

Following *Osborn* [1980], we approximate an upper limit to the turbulent diffusion coefficient by

$$K_\rho \le \frac{0.2\varepsilon}{N^2}, \qquad \text{(B2)}$$

where $N^2 = -(g/\rho_0)\partial\rho/\partial z$ and the constant 0.2 is a result of a constant flux Richardson number $Ri_f = 0.15$ in the steady state turbulent kinetic energy equation where production is balanced by dissipation and buoyancy flux. *Rohr and Van Atta* [1987] indicate that laboratory studies show 0.2 is a resonable approximation in stratified flows with Richardson numbers $R_i \ge 0.1$.

Rearranging the terms in (*B*1) and assuming that we can approximate $\partial(\rho\varepsilon)/\partial z \approx \rho\partial\varepsilon/\partial z$, we get an equation for W,

$$W = -\left(U\frac{\partial\rho/\partial x}{\partial\rho/\partial z} + V\frac{\partial\rho/\partial y}{\partial\rho/\partial z}\right) - \frac{\partial\rho}{\partial t}\Big/\frac{\partial\rho}{\partial z} + \frac{0.2}{N^2}\frac{\partial\varepsilon}{\partial z}. \qquad \text{(B3)}$$

The three main components of (B3) represent horizontal flow along sloping isopycnal surfaces, vertical displacement of isopycnals, and diapycnal mixing. From the RSVP and ADCP sections we can directly estimate all terms in (B3) except the zonal density gradient $\partial\rho/\partial x$. To this end, we use the thermal wind equations to equate horizontal isopycnal slopes in terms of vertical velocity gradients. The multiple transects result in temporal resolution sufficient to recover the mean flow and justify the use of the thermal wind approximation. Upon substitution ($(g/\rho_0)\partial\rho/\partial x = -f\partial V/\partial z$, $(g/\rho_0)\partial\rho/\partial y = f\partial U/\partial z$), we find

$$W = -\frac{f}{N^2}\left(U\frac{\partial V}{\partial z} - V\frac{\partial U}{\partial z}\right) - \frac{\partial\rho}{\partial t}\Big/\frac{\partial\rho}{\partial z} + \frac{0.2}{N^2}\frac{\partial\varepsilon}{\partial z}, \qquad \text{(B4)}$$

where the thermal wind substitution assumes that the mean velocity estimates U and V are in near geostrophic balance. We have already found that the mean zonal velocity field is reasonably explained by a simple geostrophic balance (for phase 1), and that the combined thermal wind approximations probably introduce a maximum error of only ~30% in W.

In the *Bryden* [1980] derivation a transformation of coordinates is made, and the current components (U, V) are represented in polar coordinates, say, R for current speed and θ for current direction. The first term in (B4) is then rewritten as $-(f/N^2)R^2\partial\theta/\partial z$, where R is the average current speed over the depth interval ∂z. Thus W is shown to be proportional to current veering with depth. Brydens' notation is no more intuitive than that shown in (B3) and (B4), component flow along appropriate isopycnal slope. In fact the present notation (B4) shows directly that the vertical velocities are a consequence of adjustments in the local vorticity field. The vertical shears $\partial V/\partial z$ and $\partial U/\partial z$ are the major contributions to the horizontal components of vorticity, $\xi = (\partial W/\partial y - \partial V/\partial z)$ and $\eta = (\partial U/\partial z - \partial W/\partial x)$ respectively. Therefore, the vertical velocities represented by the first term in (B4) result from horizontal advection of relative vorticity, namely $(U\partial V/\partial z - V\partial U/\partial z) \simeq -(U\xi + V\eta)$, if $|\partial U/\partial z| \gg |\partial W/\partial x|$ and $|\partial V/\partial z| \gg |\partial W/\partial y|$. A similar result is obtained by considering potential vorticity dynamics [*Levine et al.*, 1986].

The second and third terms in (B4) represent vertical displacement of isopycnals and the net vertical velocity resulting from turbulent diapycnal mixing. Vertical displacements of isopycnal surfaces may compensate for horizontal advection of tilted isopycnals but also represents locally forced upwelling and downwelling. The diapycnal mixing term does not model vertical turbulent velocities (w'), but represents the net raising of potential energy accomplished by turbulent mixing. Both of these contributions to W are estimated from the RSVP sections. The contribution $(\partial\rho/\partial t)/\langle\partial\rho/\partial z\rangle$ is estimated by first-differencing the density sections between consecutive transects, therefore obtaining seven and two estimates for phases 1 and 2, respectively. The diapycnal mixing term is estimated for each RSVP section of ε and N^2.

The first term in (B4) is calculated directly from the individual RSVP and ADCP sections of N^2, U, V, $\partial U/\partial z$, and $\partial V/\partial z$. Averaging this contribution over several realiza-

tions (transects) justifies the use of the thermal wind equations. Instantaneous estimates of W using (B4) have large nongeostrophic contributions to U and V resulting from noise like processes (e.g., inertial waves). Shown in Figure 14 is the mean W structure (in meters per day) for phase 1, formed by summing the three mean contributions. On average, the final contributions to $\langle W \rangle$ are represented by 80–90% from the flow along sloping isopycnals, 10–20% from isopycnal displacements and 0–10% from diapycnal mixing.

Acknowledgments. The authors would like to thank all those who assisted in data acquisition: Mike Neeley-Brown, Jose Baer, Ray Kreth, Terry Sullivan, Mark Willis, Pat Collier, Jane Huyer and Rich Schramm. Mike Kosro processed the shipboard ADCP data, Mark Abbott processed the AVHRR images, and Dave Reinert drafted several figures. The mooring data was provided courtesy of Bob Smith and Mike Kosro. Fruitful discussions with Dave Hebert, Jane Huyer, Mike Kosro, and Bob Smith greatly assisted in formulating ideas. The authors thank the reviewers for their helpful comments. The authors would also like to extend special thanks to the editors (K. Brink and T. Cowles) of this special issue for their comments and uncompensated time. This project was supported by the Office of Naval Research through the Coastal Sciences program (T. Kinder) under contract N00014-90-J-1215.

REFERENCES

Abbott, M., and B. Barksdale, Phytoplankton pigment patterns and wind forcing off central California, *J. Geophys. Res.*, this issue.

Bendat, J. S., and A. G. Piersol, *Random Data: Analysis and Measurement Procedures*, 566 pp., John Wiley, New York, 1986.

Bernstein, R. L., L. Breaker, and R. Whritner, California Current eddy formation: Ship, air and satellite results, *Science.*, *195*, 353—359, 1977.

Bryden, H. L., Horizontal advection of temperature for low-frequency motions, *Deep-Sea Res.*, *23*, 1165–1174, 1976.

Bryden, H. L., Geostrophic vorticity balance in mid-ocean, *J. Geophys. Res.*, *85*, 2825–2828, 1980.

Caldwell, D. R., T. M. Dillon, and J. N. Moum, The rapid-sampling vertical profiler: An evaluation, *J. Atmos. Oceanic Technol.*, *2*, 615–625, 1985.

Crawford, W. R., Pacific equatorial turbulence, *J. Phys. Oceanogr.*, *12*(10), 1137–1149, 1982.

Dewey, R. K., and J. N. Moum, Enhancement of fronts by vertical mixing, *J. Geophys. Res..*, *95*, 9433–9446, 1990.

Dillon, T. M., J. N. Moum, T. K. Chereskin, and D. R. Caldwell, Zonal momentum balance at the equator, *J. Phys. Oceanogr.*, *19*(5), 561–570, 1989.

Efron, B., Better bootstrap confidence intervals, *J. Am. Stat. Assoc.*, *80*, 171–185, 1987.

Efron, B., and G. Gong, A leisurely look at the bootstrap, the jackknife, and cross-validation, *Am. Stat.*, *37*(1), 36–48, 1983.

Flament, P., L. Armi, and L. Washburn, The evolving structure of an upwelling filament, *J. Geophys. Res.*, *90*, 11,765–11,778, 1985.

Fofonof, N. P., and M. M. Hall, Estimates of mass, momentum and kinetic energy fluxes of the Gulf Stream, *J. Phys. Oceanogr.*, *13*(10), 1868–1877, 1983.

Foreman, M. G. G., Manual for tidal currents analysis and predictions, *Pac. Mar. Sci. Rep. 78-6*, 70 pp., Inst. of Ocean Sci., Sidney, B. C., Canada, 1978.

Foreman, M. G. G., and H. J. Freeland, A comparison of techniques for tide removal from ship-mounted acoustic Doppler measurements along the southwest coast of Vancouver Island, *J. Geophys. Res.*, in press, 1991.

Freeland, H. J., and P. McIntosh, The vorticity balance on the southern British Columbia continental shelf, *Atmosphere Ocean*, *27*(4), 643–657, 1989.

Gregg, M. C., Diapycnal mixing in the thermocline: A review, *J. Geophys. Res.*, *92*, 5249–5286, 1987.

Gregg, M. C., H. Peters, J. C. Wesson, N. S. Oakey, and T. J. Shay, Intensive measurements of turbulence an shear in the equatorial undercurrent, *Nature.*, *318*, 140–144, 1985.

Haidvogel, D. B., A. Beckmann, and K. S. Hedström, Dynamical simulations of filament formation and evolution in the coastal transition zone, *J. Geophys. Res.*, this issue.

Hall, M. M., Horizontal and vertical structure of the Gulf Stream velocity field at 68°W, *J. Phys. Oceanogr.*, *16*(11), 1814–1828, 1986.

Hayward, T. L., and A. Mantyla, Physical, chemical and biological structure of a coastal eddy near Cape Mendocino, *J. Mar. Res.*, *48*, 825–850, 1990.

Hoskins, B. J., The role of potential vorticity in symmetric stability and instability, *Q. J. R. Meteorol. Soc.*, *100*, 480–482, 1974.

Hoskins, B. J., The mathematical theory of frontogenesis, *Annu. Rev. Fluid Mech.*, *14*, 131–151, 1982.

Huyer, A., Coastal upwelling in the California Current System, Prog. Oceanogr., *12*, 259–283, 1983.

Huyer, A., and P. M. Kosro, Mesoscale surveys over the shelf and slope in the upwelling region near Point Arena, California, *J. Geophys. Res.*, *92*, 1655–1681, 1987.

Huyer, A., P. M. Kosro, J. Fleischbein, S. R. Ramp, T. Stanton, L. Washburn, F. P. Chavez, T. J. Cowles, S. D. Pierce, and R. L. Smith, Currents and water masses of the coastal transition zone off northern California, June to August 1988, *J. Geophys. Res.*, this issue.

Kosro, P. M., Shipboard acoustic current profiling during the Coastal Ocean Dynamics Experiment, *SIO Ref 85-8*, 119 pp., Scripps Inst. of Oceanogr., La Jolla, Calif., 1985.

Kosro, P. M., and A. Huyer, CTD and velocity surveys of seaward jets off northern California, July 1981 and 1982, *J. Geophys. Res.*, *91*, 7680–7690, 1986.

Levine, E. R., D. N. Connors, P. C. Cornillion, and H. T. Rossby, Gulf Stream kinematics along a isopycnal float trajectory, *J. Phys. Oceanogr.*, *16*(7), 1317–1328, 1986.

McWilliams, J. C., Maps from the Mid-Ocean Dynamics Experiment, I, Geostrophic streamfunction, *J. Phys. Oceanogr.*, *6*(6), 810–827, 1976.

Moum, J. N., D. R. Caldwell, and P. J. Stabeno, Mixing and intrusions in a rotating cold-core feature off Cape Blanco, Oregon, *J. Phys. Oceanogr.*, *18*(6), 823–833, 1988.

Munk, W., F. Snodgrass, and M. Wimbush, Tides off-shore: Transition from California coastal to deep-sea waters, *Geophys. Fluid Dyn.*, *1*, 161–235, 1970.

Nishida, H., and W. B. White, Horizontal eddy fluxes of momentum and kinetic energy in the near-surface of the Kuroshio extension, *J. Phys. Oceanogr.*, *12*(2), 160–170, 1982.

Osborn, T. R., Estimates of the local rate of vertical diffusion from dissipation measurements, *J. Phys. Oceanogr.*, *10*(1), 83–89, 1980.

Paduan, J. D., and P. P. Niiler, A Lagrangian description of motion in northern California coastal transition filaments, *J. Geophys. Res.*, *95*, 18,095–18,109, 1990.

Pedlosky, J., *Geophysical Fluid Dynamics*, 624 pp., Springer-Verlag, New York, 1978.

Pond, S., and G. L. Pickard, *Introductory Dynamical Oceanography*, 241 pp., Pergamon, Elmsford, New York, 1978.

Priestley, M. B., *Spectral Analysis and Time Series*, pp. 671–681, Academic, San Diego, Calif., 1989.

Rohr, J., and C. Van Atta, Mixing efficiency in stably stratified growing turbulence, *J. Geophys. Res.*, *92*, 5481–5488, 1987.

Strub, P. T., J. S. Allen, A. Huyer, and R. L. Smith, Large-scale structure of the spring transition in the coastal ocean off western North America, *J. Geophys. Res.*, *92*, 1527–1544, 1987.

Strub, P. T., et al., The nature of the cold filaments in the California Current System, *J. Geophys. Res.*, this issue.

Walstad, L. J., J. S. Allen, P. M. Kosro, and A. Huyer, Dynamics of the coastal transition zone in 1987 through data assimilation studies, *J. Geophys. Res.*, this issue.

Washburn, L., D. C. Kadko, B. H. Jones, T. Hayward, P. M. Kosro, T. P. Stanton, S. Ramp, and T. Cowles, Water mass subduction and the transport of phytoplankton in a coastal upwelling system., *J. Geophys. Res.*, this issue.

D. R. Caldwell, J. N. Moum, C. A. Paulson, and S. D. Pierce, College of Oceanography, Oceanography Administration Building 104, Oregon State University, Corvallis, OR 97331.

R. K. Dewey, Science Applications International Corporation, 13400B Northrup Way, Suite 36, Bellevue, WA 98005.

(Received August 21, 1990;
accepted March 15, 1991.)